



## A new methodology on simulating the mechanical behavior of human renal arteries

Pomakidou S.,<sup>1</sup> Kourkoulis, S.,<sup>2</sup>

1. National Technical University of Athens, Laboratory of Testing Materials, Greece E-mail: [spomakidou@outlook.com](mailto:spomakidou@outlook.com)

2. National Technical University of Athens, Laboratory of Testing Materials, Greece

### Abstract

Arterial stiffness has emerged and is established as a vascular biomarker with potentially high prognostic value when determining cardiovascular risk. There is a high demand for comprehensive experimental research and mathematical modeling of renal artery mechanics which would best explain their mechanical behavior. The aim of this study is to understand how the renal artery behaves under a tension stress condition and reproduce it through a mathematical and computational approach. Human cadaveric arteries are tested in 3D inflation-extension biomechanical experiments; first generation data (i.e. external diameter, lumen pressure, axial force) are transformed, via continuum mechanics formulation, into second generation data (i.e. circumferential stress, axial stress, circumferential strain in no load state). Following the response of the phenomenological functions, a computational model is validated to detect the overall properties of a user defined hyper-elastic material for structural simulation in human renal arteries tissues. The results of this study can be used as engineering methods in clinical practice by providing a surgeon/interventionist the data required to efficiently plan and implement procedures. Also, comparing different techniques by simulated models enables spotting any problems of in vivo situations and optimization of surgical methodologies.

Keywords: 3D inflation-extension, ANSYS simulative model, human renal artery, hyper-elastic models

## 1. Introduction

The renal arteries, which constitute the only vascular supply to the kidneys, are paired arteries arising from the lateral side of the abdominal aorta below the level of the superior mesenteric artery at the upper lumbar level. A renal artery enters the kidney through the hilum which is located where the kidneys curve inward into a concave shape. Normally, the renal artery splits into two main branches, each in turn, splitting into numerous segmental arteries delivering blood to different areas of the kidneys (Gulas et al., 2018; Leslie & Sajjad, 2019).

The abdominal aorta and its branches are of utmost importance in the blood distribution system and any abnormal function of these vessels could consequently cause problems to organs directly connected with them. One particularity of the renal microcirculation is that the excretory performance of the kidneys is closely associated to the intra-renal haemodynamics (Chade, 2014). This, in combination with the exposure of the kidney microvasculature to variations or abnormalities in blood flow through the macro-microvascular interaction (Climie et al., 2019), highlights the role of the renal artery in the overall kidney function.

Despite the plethora of studies investigating the mechanical properties of large blood vessels, few have focused on the renal arteries. The need for understanding the renal artery mechanical behaviour has been increasingly acknowledged, not only for its direct relationship with kidney function but also due to the extended implications to the overall health. The extent and severity of renal artery pathology has been argued to be reflective of the overall atherosclerotic burden (Textor et al., 2009). Renovascular disease, which is mainly associated with atherosclerotic renal artery stenosis, is accompanied by reduced perfusion of the kidney and is a major cause for hypertension development. Renovascular hypertension has been reported among the most common underlying etiologies of secondary forms of hypertension and of treatment-resistant hypertension (Hermann and Textor, 2018). Renal haemodynamic state is linked to the vascular nature of the kidney and, thus, closely related to the systemic circulation. It has been demonstrated that renal haemodynamics and arterial stiffness are associated in patients with renal disease but also in patients with elevated blood pressure only (Calabia et al., 2014).

Arterial stiffness has emerged and is being established as a vascular biomarker with potentially high prognostic value when determining cardiovascular risk and identifying early vascular disease (Zanoli et al., 2019). The importance of gaining insights into the mechanical behaviour of the micro and macro – vasculature is becoming even more profound when considering the projections from the American Heart Association which states that “by 2035 almost half of the US population will suffer a cardiovascular disease while the total direct and indirect costs will soar, exceeding \$1 trillion” (American Heart Association, 2017).

Since the '90s much research has been dedicated to the biomechanics of the arterial wall, with seminal publications improving our understanding and introducing new approaches (Fung 1993; Humphrey 2002). Different methods have been employed to characterize the mechanical properties of blood vessels, including, but not limited to, in vitro tensile testing, non-invasive in

vivo vascular ultrasound and mathematical models (Butlin et al., 2020; Vappou et al., 2010). Working on porcine artery specimens, Avril et al. (2013) have proposed a biomechanical model that predicts the relationship between axial force and internal pressure and discussed the implications of the orientation and deposition of collagen fibers. Another study by Zhou et al (2014) has applied an experimental and theoretical approach to quantify the passive mechanical response of the primary porcine renal artery and develop a model facilitating the calculation of stress and strains under physiological loading.

Clearly, there is an increasing demand for comprehensive experimental research and mathematical modeling of renal artery mechanics which would better explain the overall mechanical behavior. To the authors knowledge, there are no reports in the literature on the human renal artery mechanical properties, neither a mathematical formulation for stresses and strains nor a computational simulation to topologically describe stress and strain allocation as well as predicting tensors in high perming loads.

The main objective of this study is two-fold; first, to determine and validate a mechanical model that can describe the renal artery mechanical properties and, second, to enrich material libraries with a biomaterial that can simulate real-life tissue behavior. Furthermore, the constructed model could be a valuable tool for the definition of critical stress-strain tensors that generate pathogens in renal arteries.

Within this scope, human cadaveric arteries are tested in 3D inflation-extension biomechanical experiments; first generation data (i.e. external diameter, lumen pressure, axial force) are transformed, via continuum mechanics formulation, into second generation data (i.e. circumferential stress, axial stress, circumferential strain in no load state). Furthermore, the implementation of Strain Energy Density (SED) phenomenological functions were utilized to adopt the optimal SED for renal arteries and validate the modeled vs. experimental data with phenomenological functions. Finally, a computational model is developed with the state-of-the-art finite element code ANSYS, exploiting the above experimental data in conjunction with second generation data.

## 2. Materials and methods

### 2.1 Experimental Procedure

#### 2.1.1 Tissue specimens and morphometric measurements

Seventeen human renal arteries (9 left and 8 right) were used for the experimental part of this study. The specimens were received from the abdominal aorta (Figure 1, left) of 11 human cadavers; metadata information is provided in Table A1 of Appendix 1. Arteries were then dissected, appearing as cylindrical tubes (Figure 1, right) and were gently trimmed of adjacent tissues, taking care to leave as much of adventitia intact. The *ex situ* segment length was within the range of 5-10 mm.



**Figure 1: Fresh abdominal aorta from a 24 years old male after cleaning adherent tissues**

It is known that the state in which the artery is excised from the body is not a stress-free state; when the arterial ring of circular geometry (no load state, NLS) is cut in the radial direction, it springs open into an open sector (zero stress state, ZSS), characterized by an opening angle. The angle formed by two radii drawn from the inner wall's midpoint to the open sector's inner wall tips is known as the opening angle (Guo et al., 2005). Rings were laid in a Petri dish containing calcium-free Krebs solution at 37.8°C and photos were taken by a digital camera (model E400; Olympus Optical Co. Ltd, Tokyo, Japan) under a stereomicroscope (Stemi 2000C; Carl Zeiss Optical, Chester, VA, USA), at two different time-points: a. at NLS, and b. at the ZSS, 30 minutes after the radial cut.

The morphometric characteristics including circumferential length of outer and inner wall, wall thickness and opening angle, were assessed with an image analysis software (Image-Pro Plus v.4.5; Media Cybernetics Inc, Silver Spring, MD, USA). Residual strains were calculated for the inner and outer arterial wall by the ratio of the respective circumferential length in the NLS over the circumferential length in the ZSS.

### 2.1.2 Extension-Inflation experimental procedure

The extension-inflation experimental procedure was conducted as described in Sokolis (2012). The experimental set-up is shown in Figure 2. The renal arteries segments were cannulated at their ends with stainless steel catheters. They were filled with calcium-free Krebs solution, including 0.25% EGTA, and put horizontally in a bath containing the same fluid, which was set to 37.8°C and aerated with carbogen at pH=7.4.

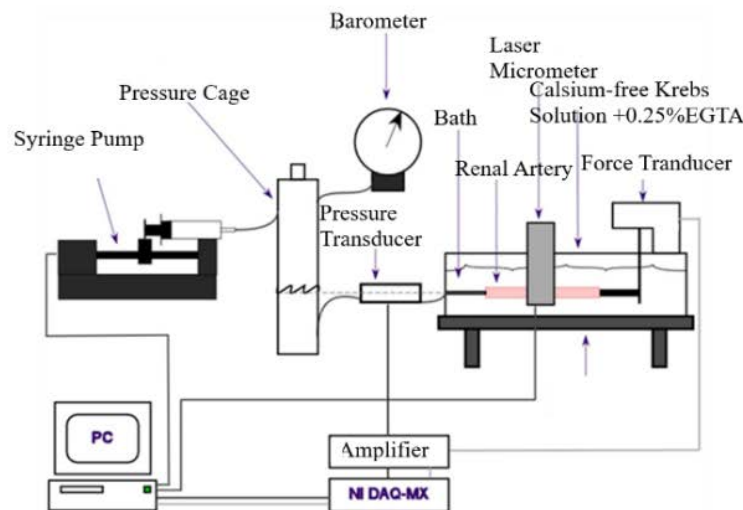


**Figure 2: The experimental set-up used for the inflation-extension testing**

At one end, the catheter was stationary, while at the other end, it was attached to a force transducer (Fort 100; World Precision Instruments, Hertfordshire, UK), recording the longitudinal force with an accuracy of 0.25 g. This catheter was suspended from a micrometer (Tesa Technology, Renens, Switzerland), permitting longitudinal extension of the renal arteries from 120% to 160%, in 10% increments. Length measurements as the separation distances between catheters were justified by the large segments aspect ratio, i.e. average length to external diameter, presumably making unimportant the errors caused by edge effects.

Renal artery segments were extended from 100% to 160% of their in-situ length and then submitted to inflation while their length was kept fixed during pressurization. The lumen of the renal arteries segments was inflated/deflated in the range of 0–200 mmHg pressure with a step rate of 0.15 mmHg/s, and sensed by a transducer (BLPR; World Precision Instruments) with an accuracy of 0.5 mmHg. The external radius was continuously monitored at the central portion by a laser micrometer (LS-3100; Keyence Corp., Osaka, Japan), with 1 mm accuracy.

Five loading–unloading cycles served for preconditioning. Preliminary tests not shown within this paper demonstrated that preconditioning and the ensuing inflation/extension testing had no effect on the NLS and ZSS geometry of the renal artery specimens, including their opening

angle, therefore, validating the use of non-preconditioned specimens for the determination of residual strains. Data was amplified and stored on an accompanying computer using an acquisition interface (Labview v7.1; National Instruments, Austin, TX, USA).

### 2.1.3 1<sup>st</sup> generation data

First generation data were produced based on the experimental procedure. The renal artery wall is treated as a single, homogeneous cylinder, ignoring its layered structure, which includes an intimal, medial, and adventitial layer, which is beyond the scope of this study (Sokolis et al., 2013). The kinematic equations under longitudinal extension and lumen pressure, are shown in the Appendix 2.1.

### 2.1.4 Identification of material parameters

In order to describe the mechanical properties from the experimental procedure it was necessary to compute the material parameters, which was achieved by fitting equations (see section 2.1.6) to pressure–radius–force data with user-defined C-routines programmed in MicroCal Origin (v7.5; OriginLab Corp., Northampton, MA, USA), via a least-squares Simplex algorithm. All simulations pertained to loading data, substantiated by the little measurable hysteresis. The parameter values were restrained by inequalities of thermodynamic origin, ensuring physically realistic values and SEF (Strain Energy Function) positivity. The objective function minimized the normalized squared differences between the experimental data and model predictions. Data were considered every 0.5 mmHg, from 1 to 200, encompassing a number of 600 data points for all stretch ratios. Optimization was repeated for various initial parameters to ensure global rather than local extrema, which is a common problem with multivariate nonlinear optimization. To facilitate the selection of proper initial parameter values for the biphasic models, the low-pressure data were fitted first using only the quadratic terms of the below Equations in section 2.1.5, and then was the entire data set fitted by both terms of the two-term SEF. The goodness of fit was estimated by the root-mean-square (RMS) error  $\epsilon$  and over-parameterization.

### 2.1.5 Phenomenological Model - Strain Energy Density Functions

The aforementioned experimental data of this study were fitted with a quadratic (orthotropic) and exponential (orthotropic) SEF, proposed by Zhou & Fung (1997):

$$W = q + K(e^Q - 1), \quad q = b_{\theta\theta} E_{\theta}^2 + b_{zz} E_z^2 + b_{\theta z} E_{\theta} E_z,$$

*Equation 1 Fung Quadratic SEF*

which is based in Fung and Neo-Hookean (isotropic) - exponential (orthotropic) SEF as presented in the following equations.

Fung SEF is expressed via Green strains  $E_{\theta}$  and  $E_z$  in the  $\theta$  and  $z$  directions as below (Fung et al., 1979):

$$W = K(e^Q - 1), \quad Q = c_{\theta\theta} E_{\theta}^2 + c_{zz} E_z^2 + c_{\theta z} E_{\theta} E_z,$$

*Equation 2 Fung SEF*

where  $c_{\theta\theta}$ ,  $c_{zz}$ , and  $c_{\theta z}$  (non-dimensional) are the material parameters and K is a scaling factor.

The neo-Hookean (isotropic) and exponential (orthotropic) SEF is postulated for large elastic arteries by Weizsäcker et. al (1988 & 1995):

$$W = \mu(I_1 - 3) + K(e^Q - 1),$$

*Equation 3 Neo-Hookean SEF*

where  $\mu$  is a stress-like parameter,  $I_1 = \text{tr}C$  is the first invariant of the right Cauchy–Green strain tensor,  $C=2E+I$  and Q is the quadratic function (Sokolis et al., 2013).

### 2.1.6 2<sup>nd</sup> generation data

After the computation of material parameters using the aforementioned SEF, the 2<sup>nd</sup> generation data are produced using the equations in Appendix 2, which will also be used in the simulation part of this study. A direct enforcement of incompressibility allowed the consideration of a SEF that is a 2D function of circumferential and longitudinal strains as a constitutive descriptor in the general thick-walled setting (Li et al., 2018).

## 2.2 Simulation Procedure

The material behavior was simulated using a 3D engineering simulation software, ANSYS software package (ANSYS, 19.2). In this section, the simulation procedure is briefly described, including the 3D geometrical model used and some essential theoretical background for the simulation, the boundary conditions and the numerical computations.

Since blood flow simulation is out of the scope of the present study, and the focus is placed on how the structural part of an artery is acting to external forces, the fluid simulation domain in the model is suppressed, additionally saving computational time and resources.

### 2.2.1 Geometry

The geometry used for the simulation is that of a symmetrical cylindrical tube with the same length as the real artery specimens and uniform thickness along the entire length. The 3D model used for the simulation was generated by the Design Modeler CAD module of ANSYS software. We adopted the Cartesian coordinate system with z axis assigned for longitude. The length of the modeled artery was set at  $L=15\text{mm}$ , the external radius at  $R_{\text{outer}}=3.63\text{ mm}$  and the thickness at  $t=1.18\text{ mm}$ . The prescribed model refers to a random sample and represents the solid domain  $\Omega_s$ , which is divided in five parts: the solid body, the inner surface of the cylinder, the outer surface and the two cross section areas normal to z axis of global coordinate system shown in Figure A1 (Appendix 3).

## 2.2.2 Incompressibility Factor

The behavior of a human tissue could be approached with a near-incompressible, isotropic hyperelastic material (Scotti et al., 2008). When a material like this deforms, its volume is maintained due to mass conservation in conjunction with the unchanged material density. This is why the third invariant  $I_3$  of the Cauchy-Green deformation tensor, is taken equal to 1 and the strain-energy function can be expressed as a function of invariants  $I_1$  and  $I_2$ .

A hyperelastic material could reveal stretch-locking effects during its deformation, in which the molecular chains are under maximum strain rates. In order to prevent such an effect during simulation in commercial software like ANSYS, the invariant  $I_3$  is not suppressed but is taken into account in the strain-energy function. This consideration adds a small compressibility factor  $D$ , defined as follows:

$$D = \frac{3(1 - 2\nu)}{E}$$

where  $\nu$  is the Poisson ratio and  $E$  the Young modulus. This is directly related with the bulk modulus  $K$  as shown below.

$$K = \frac{1}{D}$$

In order to prevent a stretch locking situation in simulation, the  $K$  factor must be prevented from being infinity, so the Poisson ratio tends to a value of 0.5, in order the  $D$  factor not to be zero.

## 2.2.3 Hyperelastic model

The artery wall is assumed as a non-linear, orthotropic material with hyperelastic characteristics and near-incompressible behavior with a density of  $\rho_w=1.2\text{g/cm}^3$  (Scotti et al., 2008). The wall tissue represented in this work has average characteristics of a hyperelastic material that was reproduced from our experimental data.

In order to reproduce a material with the prescribed behavior, it is necessary to choose a suitable model for the strain energy function. The Mooney – Rivlin model is a hyperelastic material model, which uses the first and second invariant

of the left Cauchy-Green deformation tensor. The aforementioned fit took place using a Mooney-Rivlin model of 5 parameters for the strain-energy density function (ANSYS, 19.2) shown below:

$$W = \sum_{p,q=0}^N C_{pq} (I_1 - 3)^p (I_2 - 3)^q \text{ }_{\text{Deviatoric}} + \sum_{m=1}^1 \frac{1}{D_m} (J - 1)^{2m} \text{ }_{\text{Volumetric}}$$

where  $C_{pq}$  are the material constants which are computed from the curve fitting module using uniaxial and biaxial experimental data, available in ANSYS software. The strain energy function has two terms, the deviatoric which is responsible for the material deformation and the volumetric which is related with the volumetric strain in order to approach the near incompressible behavior. This model was chosen due its ability to estimate strain conditions with local values at about 200% and its good approximation using biaxial test results (Kim et al., 2012).

### 2.2.4 Experimental Data Fitting

In order to use the model described in the above section, the ANSYS software prerequisites experimental data. The fitting curve module can use uniaxial and biaxial data in order to fit a curve from which a user defined material behavior can be described.

The curves that were produced from the experimental axial and circumferential stress ( $\sigma_z$  and  $\sigma_{th}$ ) to circumferential strain ( $\epsilon_{th}$ ) are used as uniaxial and biaxial data respectively. The fitting curve module of ANSYS software performs a least squares analysis, from which the Mooney-Rivlin constants can be determined using experimental data. In this analysis the sum of squared error between experimental and Cauchy stresses values is minimized, according to the function below (ANSYS, 19.2):

$$E = \sum_{i=1}^n (T_i^E - T_i(C_j))^2$$

where E is the least squares residual,  $T_i^E$  the experimental stress values,  $T_i(C_j)$  engineering stress values as function of the Mooney-Rivlin constants and n the number of the experimental data points.

As the above equation minimized by setting the variation of the squared residual  $\delta E^2$  to zero, a set of equations in the form  $\partial E^2 / \partial C_j = 0$  can be used to compute the Mooney-Rivlin constants.

The material curve that was produced after the experimental data fit in ANSYS is presented in Figure 3.

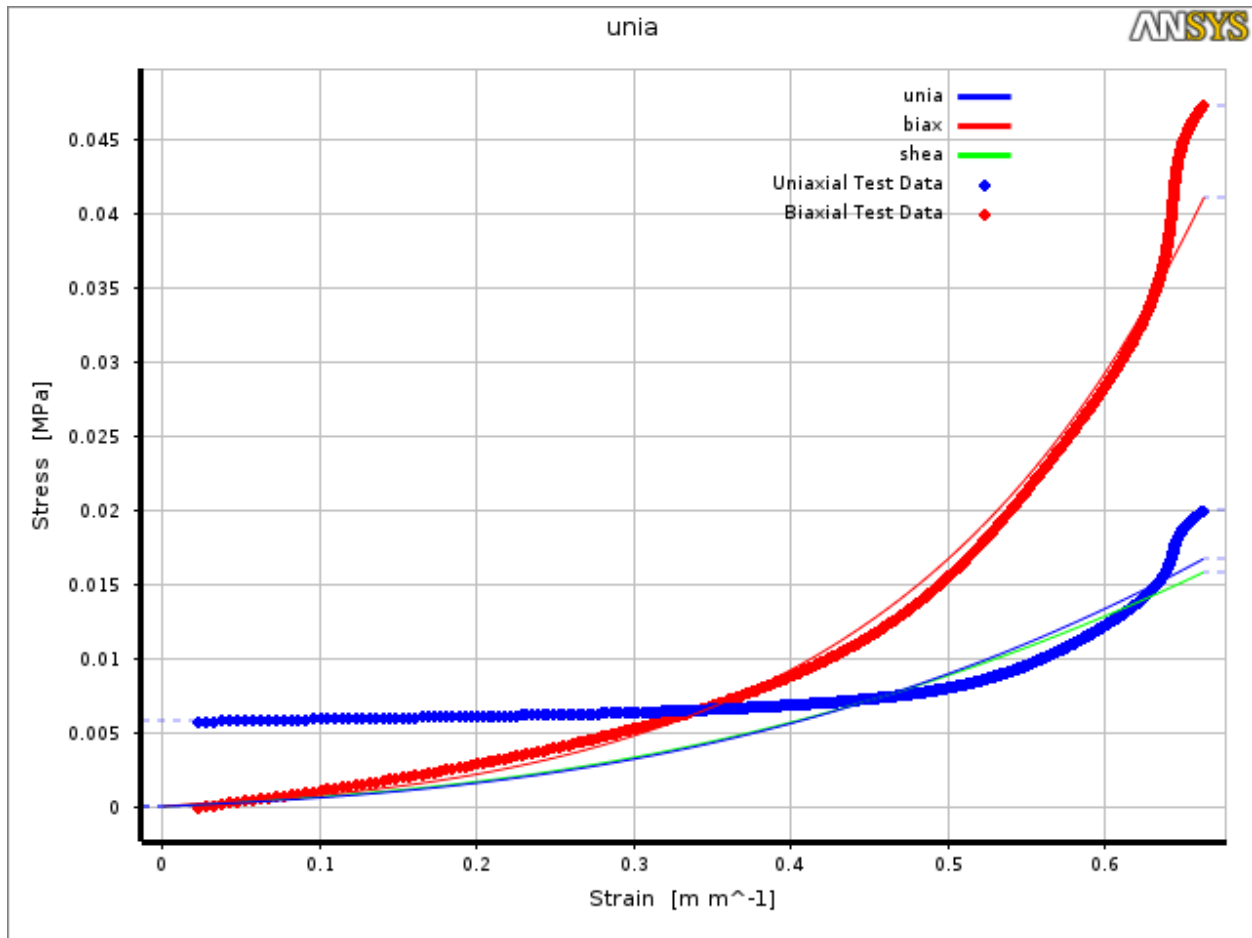


**Figure 3: Material curve fitting in ANSYS Software**

The Mooney-Rivlin constants that are calculated after the curve fitting procedure are shown in Table 1.

**Table 1: Material constants obtained from the Mooney-Rivlin function.** The incompressibility parameter is manually inserted as a value very close to, but not equal to, zero, in order to simulate the near-incompressible behavior with a Poisson ratio of 0,49999.

Material Constant C10 (Pa)	2581.304
Material Constant C01 (Pa)	-1792.49
Material Constant C20 (Pa)	4235.106
Material Constant C11 (Pa)	-3346.19
Material Constant C02 (Pa)	1193.273
Incompressibility Parameter D1 (Pa <sup>-1</sup> )	-1.00E-05

### 2.2.6 Domain Discretization

The numerical solution is computed through the finite element method (FEM) in the solid domain, used in ANSYS software (ANSYS, 19.2). The hexahedral meshing method was chosen

due to axisymmetric geometry and its simplicity but also because it outweighs an unstructured mesh on computational time and memory cost.

The model is composed of 395560 linear, hexahedral elements with eight nodes per element and 434496 nodes in total. A mesh sensitivity analysis is described in section 3.2.2 explaining the adequacy of the selected mesh size. This mesh achieves a balance between CPU simulation time and results in errors in contrast to using a finer mesh, and it is shown in Figure 4.

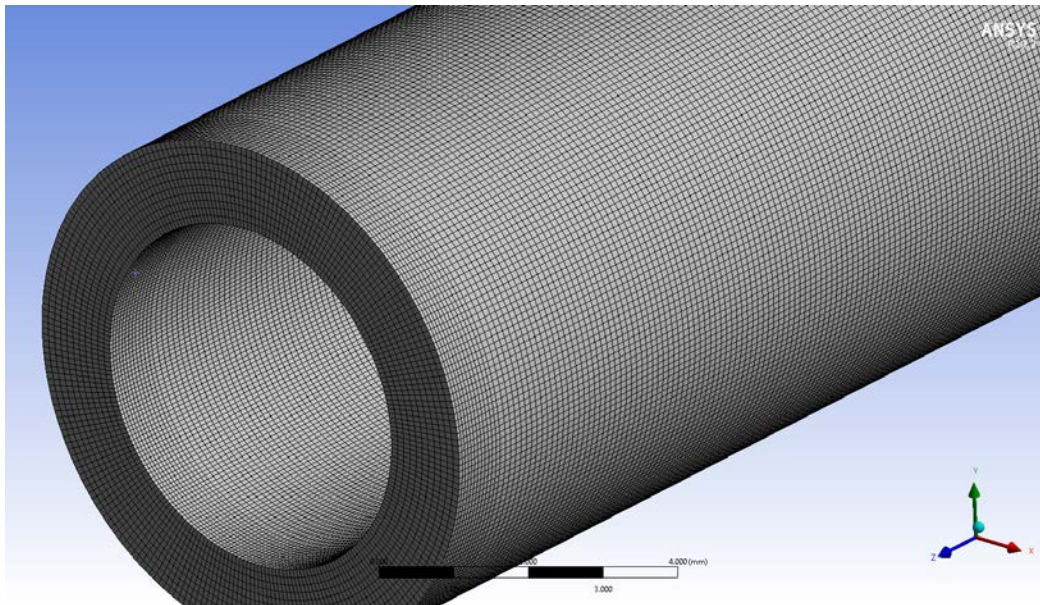


**Figure 4: Computational domain discretization**

The represented mesh is generated through the ANSYS mesh module (ANSYS, 19.2). A multizone method is used in conjunction with an edge sizing limitation for the inner circular edges of the model and an inflation method for the circular cross sections of the cylinder as shown above.

The numerical simulation of a hyperelastic near incompressible material could reveal problems like shear or volumetric locking. The shear-locking (Stolarski, 1983) is a problem based on geometric model characteristics and can be overcome with a finer mesh at the affected areas. However, a volumetric locking (Wells et al., 2002) is a numerical problem which occurs due to material property and can be dealt, using an element type that can anticipate with the code locking problem. From element scope and during deformation the volume must be maintained in order to simulate an incompressible or near incompressible material behavior. This is achieved through an internal hydrostatic pressure  $P$  of the material which is used to establish an equilibrium of the equations which involves the displacements  $u$  and the external loads  $F$ , as it is shown below.

$$[K_{uu} \ K_{uP} \ K_{Pu} \ K_{PP}] \begin{pmatrix} \Delta_u \\ \Delta_P \end{pmatrix} = \begin{pmatrix} \Delta_F \\ 0 \end{pmatrix}$$

Thus, such a kind of simulation demands the use of an element with a mixed u-p formulation capability (Scotti, 2008; Stolarski, 1983). Thus, a Solid185 element type, according to ANSYS

shortage (ANSYS, 19.2), is applied to finite elements in order to generate the solution matrix of the equations as shown in Figure 5.

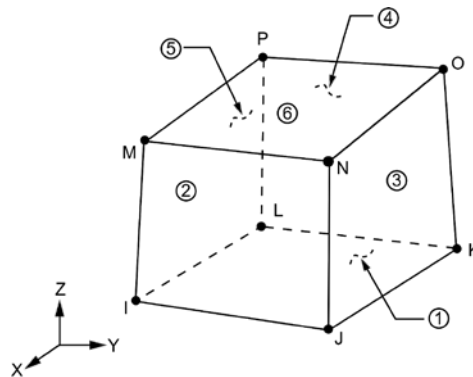


**Figure 5: Solution matrix**

This element is preferred due to its capability to deal with hyperelastic behavior with large strains. It is also suitable for mixed u-p formulation where u is the corresponding displacement and p the internal hydrostatic pressure that is generated in a hyperelastic material during its deformation in order to simulate deformations of near incompressible materials such as an artery wall. Further from the volume conservation, this element uses a selective reduced integration method, known as B-bar method, which handles shear and volumetric locking phenomena in such kind of simulations (ANSYS, 19.2).

### **2.2.7 Simulation Procedure**

The simulation procedure is separated in two parts. The first part includes the displacement where the cylindrical model is lengthened along the z axis under specific boundary conditions, and the second refers to the applied pressure where the model is stretched to its final state according to the modified boundary conditions and the applied external loads.

### **2.2.8 Boundary Conditions**

During the first step of the simulation procedure, the cylindrical model is stretched along the z – axis. In order to achieve this deformation two kinds of boundary conditions are applied to the cylinder: a fixed support and a displacement one, as set by other studies (Scotti, 2008). The former is applied to the cross-sectional area normal to plane  $z=0$  and the latter to the opposite cross-sectional area normal to  $z=15\text{mm}$ . The displacement support Degrees of Freedom (DOFs) are restricted to zero along x- and y- axis and are free for movement along  $z>15\text{mm}$  according to user input. The deformation takes place in one step and after the completion of this the DOFs are locked to the final position for the steps that will follow. The boundary conditions for this step are illustrated in Figure 6.

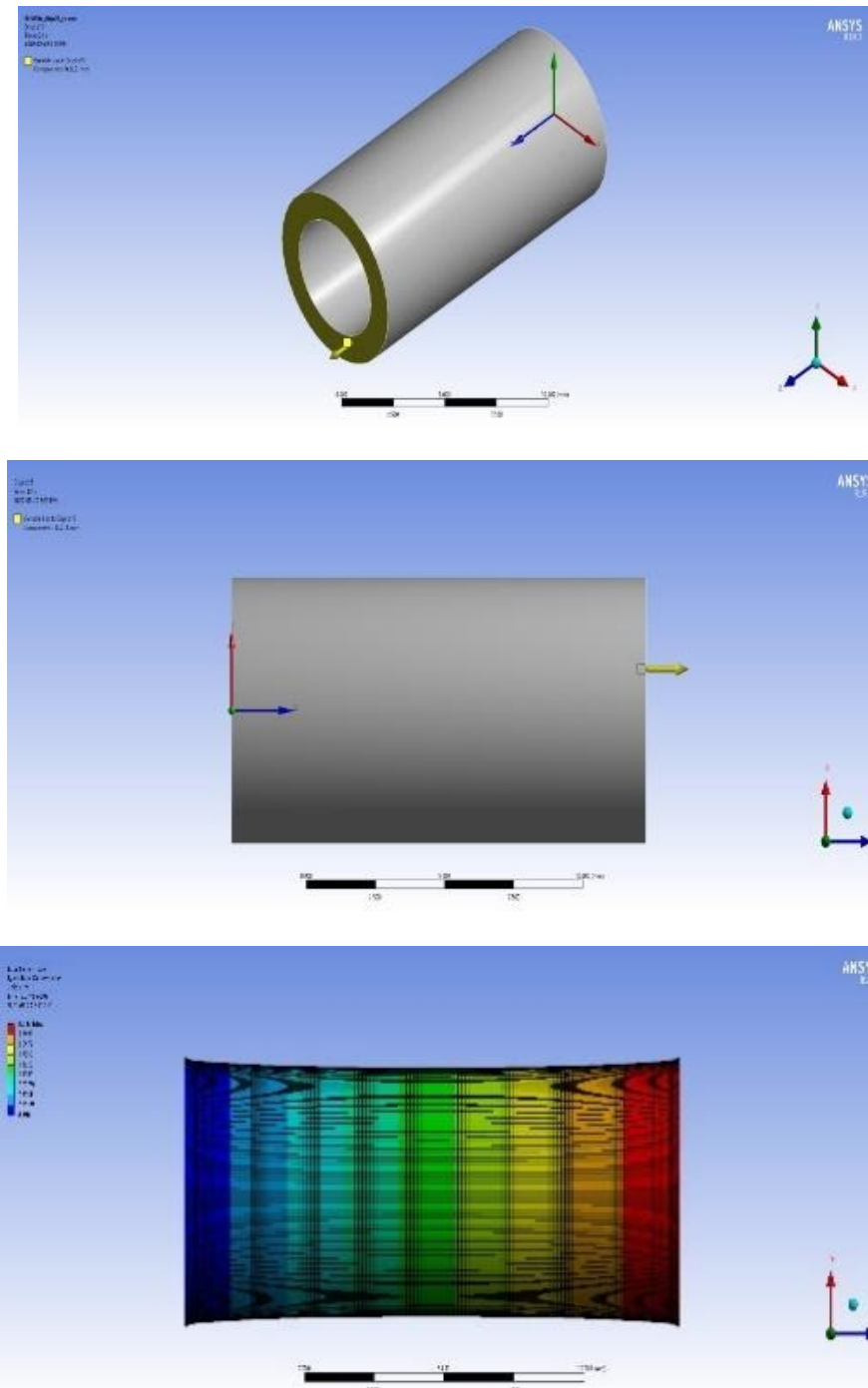


**Figure 6: 1<sup>st</sup> step boundary conditions (top), 1<sup>st</sup> step pre-deformation state (middle) and 1<sup>st</sup> step after deformation state (bottom)**

The 1<sup>st</sup> step solution is taken as a starting point for the 2<sup>nd</sup> step where the previous boundary conditions are suppressed and new are applied. In order for the fluid domain to be suppressed in the simulation, a pressure across the inner surface of the artery wall was applied. The model is also fixed to the global coordinate system with two fixed supports, one per inner edge of the cross-sectional areas as shown in Figure 7.

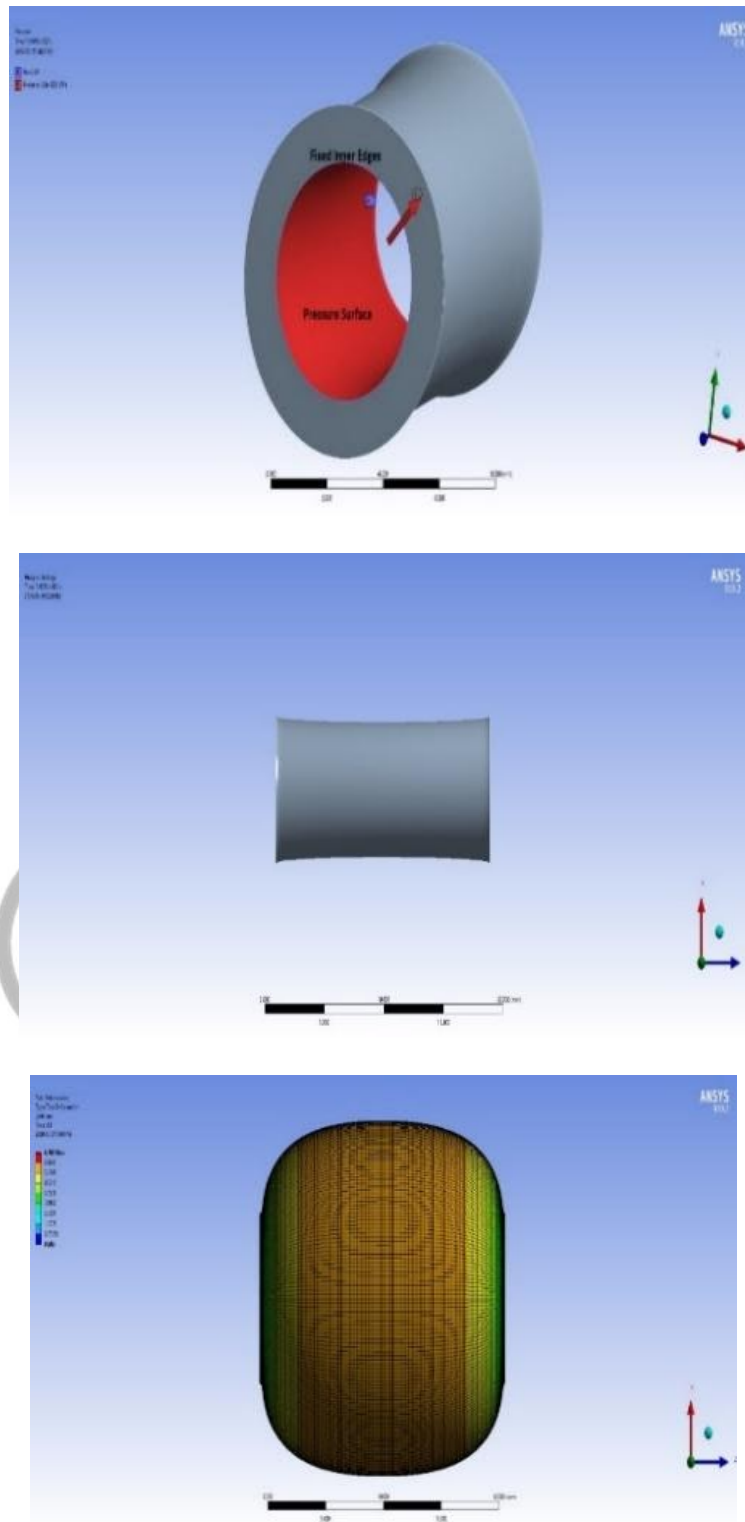


**Figure 7: 2<sup>nd</sup> step boundary conditions (top), 2<sup>nd</sup> step pre-deformation state (middle), 2<sup>nd</sup> step post- deformation state (bottom)**

## 2.2.9 Numerical computation

As a static structural problem, solution is evaluated in sub-steps through an iterative procedure, until a desirable level of convergence is achieved. The matrix form of the equations is as follows.

$$[K]\{u\} = \{F^a\}$$

where K the stiffness matrix, u the displacement vector and  $F^a$  the applied loads vector. The stiffness matrix is a function of the unknown vector u so the above expression is a set of nonlinear equations. In this study, the Newton-Raphson iterative method (Scotti, 2008) was deployed to solve the nonlinear equations. According to this method, the following set of equations was used:

$$\begin{aligned} [K_i^T]\{\Delta u_i\} &= \{F^a\} - \{F_i^{nr}\} \\ \{u_{i+1}\} &= \{u_i\} + \{\Delta u_i\} \end{aligned}$$

Where, i is the current equilibrium iteration,  $K_i^T$  the Jacobian matrix and  $F_i^{nr}$  the vector of restoring loads corresponding to element internal loads. Both of them are computed from the u vector in i iteration. The right-hand side is the residual out of balance load vector as the system is out of equilibrium. The convergence criteria are set to the order of magnitude of  $10^{-4}$  for the displacements and forces.

## 2.3 Statistical analysis

The normality of the distribution of continuous variables was assessed using the Shapiro-Wilk test. For the morphometric results, comparisons between two groups were performed by two-tailed Student's t-test, using the SPSS software for Windows, version 16.0. (SPSS Inc, Chicago, IL, USA) Variables are presented as mean  $\pm$  standard error (SE), unless otherwise stated. Bivariate associations were analyzed using Pearson R correlation. For the validation of model to experimental data, the nonlinear regression software package inside MicroCal Origin (v7.5; OriginLabw, Corp., Northampton, MA, USA) The two-tailed t-test and ANOVA followed by the Bonferroni post hoc test were used to test for directional differences in 3D models, respectively. Post-hoc multiple comparisons were also performed with Tukey test. Statistical significance was defined as  $p < 0.05$ .

## 3. Results

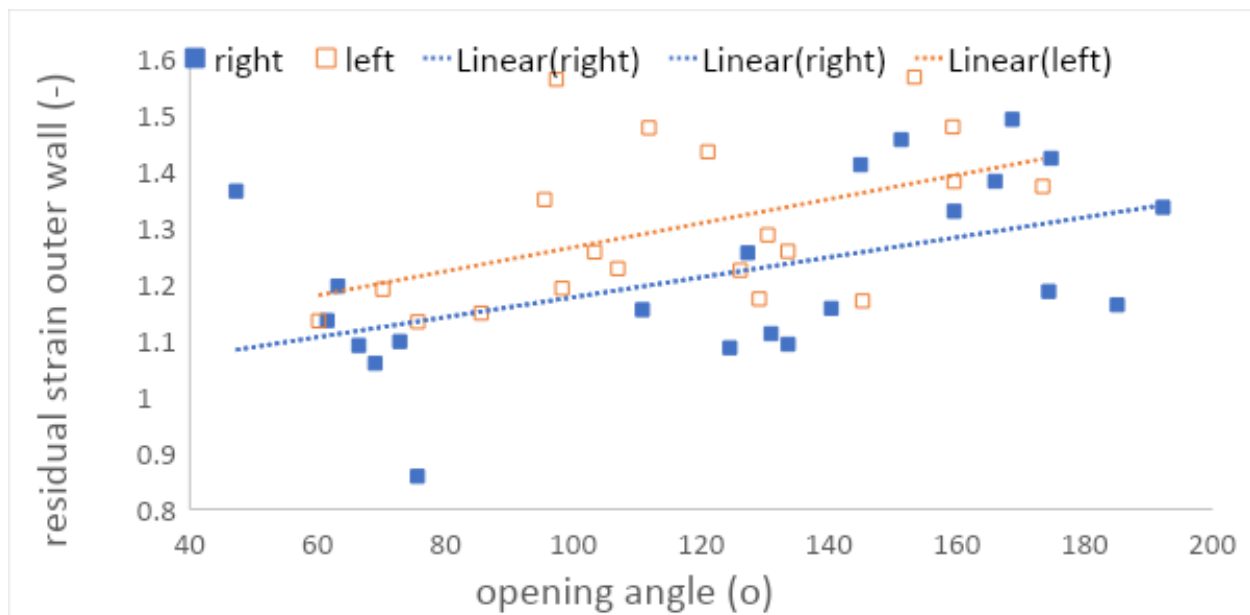
### 3.1 Experimental Results

#### 3.1.1 Morphometric results

After radial incision of the ring specimens, the mean opening angle of the arteries open sectors was found  $121 \pm 6^\circ$ . When examining the left and right renal arteries separately, the mean

opening angle was  $117 \pm 7^\circ$  and  $125 \pm 10^\circ$ , respectively, although no statistically significant difference was detected between the two groups.

Figure 8, top, depicts the scatterplot showing the correlation between the residual strain in the outer wall with differing opening angle for the left and the right renal arteries, separately. Outer wall residual strains showed a strong positive correlation with opening angle (OA) for the total of arteries ( $r=0.451$ ,  $p=0.003$ ) (trendline not shown in plot) as well as for both left renal arteries ( $r=0.476$ ,  $p=0.034$ ) and right renal arteries ( $r=0.514$ ,  $p=0.014$ ), separately. In order to illustrate any difference in the relationship of the opening angle with the contribution of inner and outer surface residual strains, the residual strain difference (outer minus inner residual strains) is plotted over the opening angle values in Figure 8, bottom. The difference in residual strain was strongly positively correlated with OA for both left ( $r=0.521$ ,  $p=0.018$ ) and right ( $r=0.502$ ,  $p=0.017$ ) renal arteries. Elevation of the OA is accompanied by a greater increase in the residual strain of the outer wall than that of the inner wall.



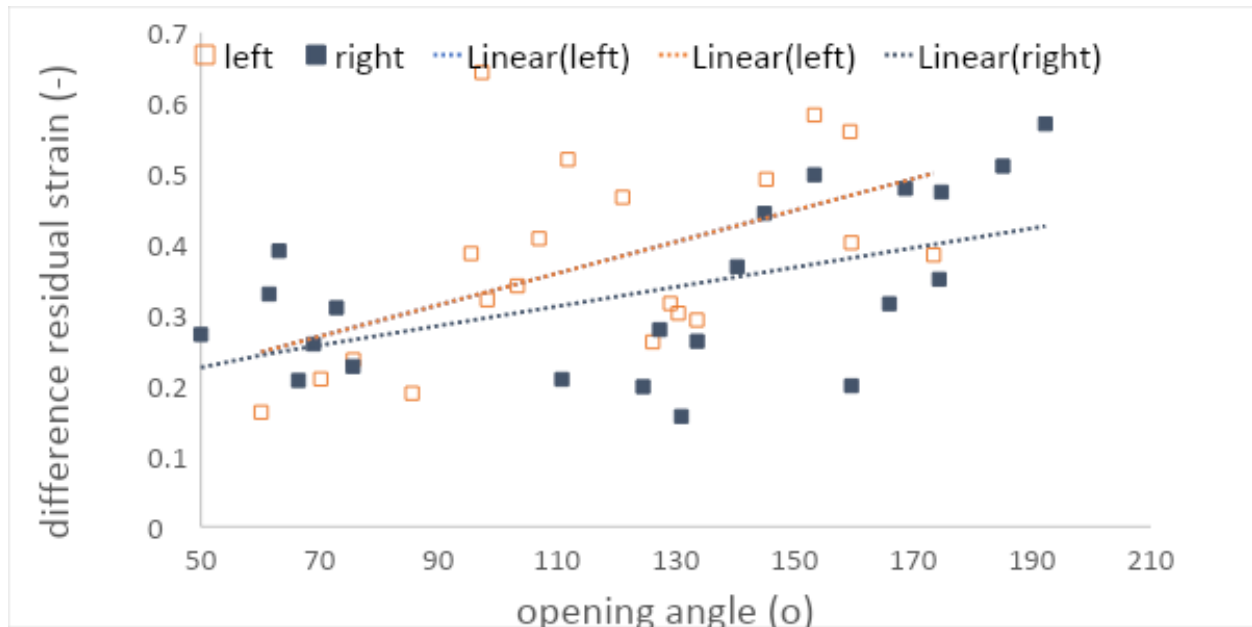


**Figure 8: Residual strain in outer wall (top) and difference in residual strain (outer-inner) (bottom), with differing opening angle**

When examining the male and female samples, separately, no significant correlation was found between the difference in residual strain and the OA, although there has been a trend for a moderate correlation in female samples ( $r=0.382$ ,  $p=0.097$ ).

On the total of samples, OA was strongly negatively correlated with increasing age ( $r= - 0.667$ ,  $p=0.035$ ). Interestingly, a very strong correlation pattern was detected within the right artery samples ( $r= - 0.842$ ,  $p=0.002$ ), while no correlation was found for the left arteries. The respective scatterplots are shown in Figure 9. When examining the correlation between OA and age for the female and male specimens separately, no correlation was detected. Arterial thickness did not reveal any significant correlation with opening angle in neither male nor female subjects.

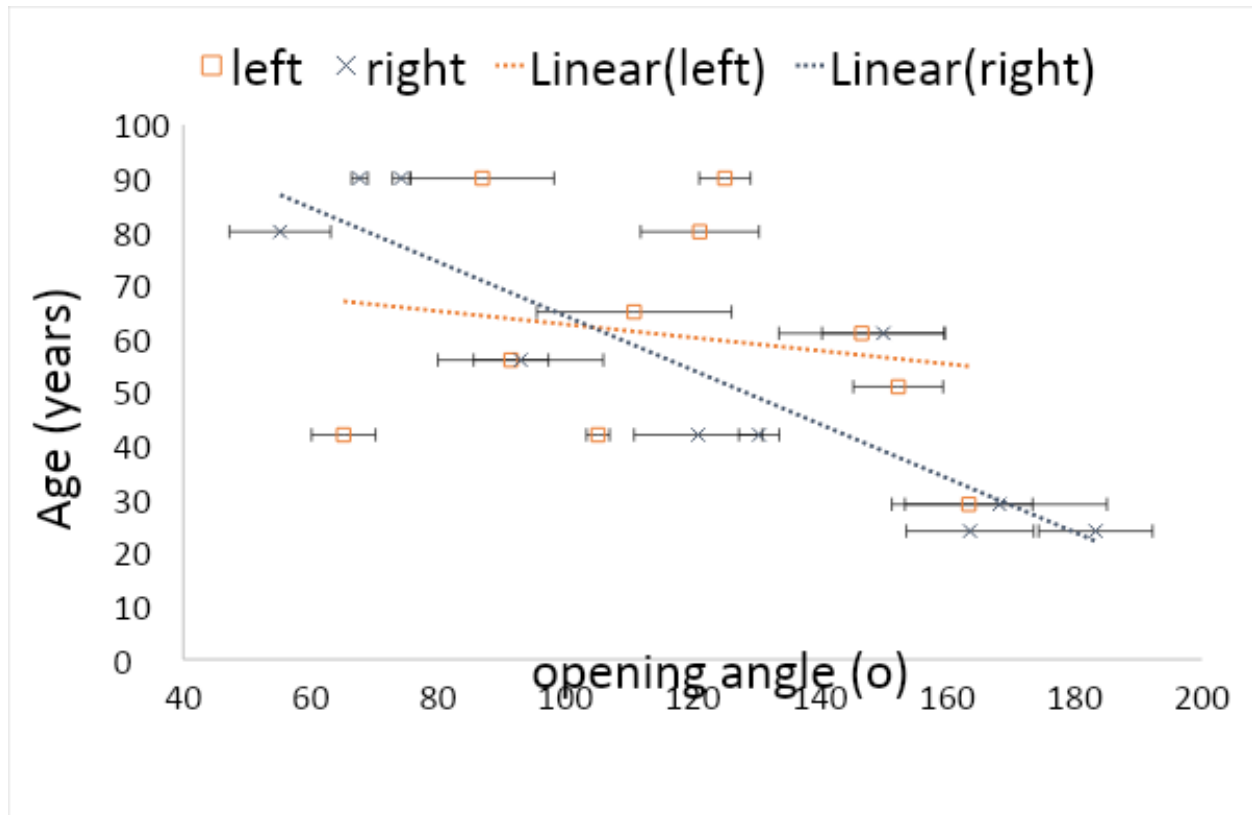
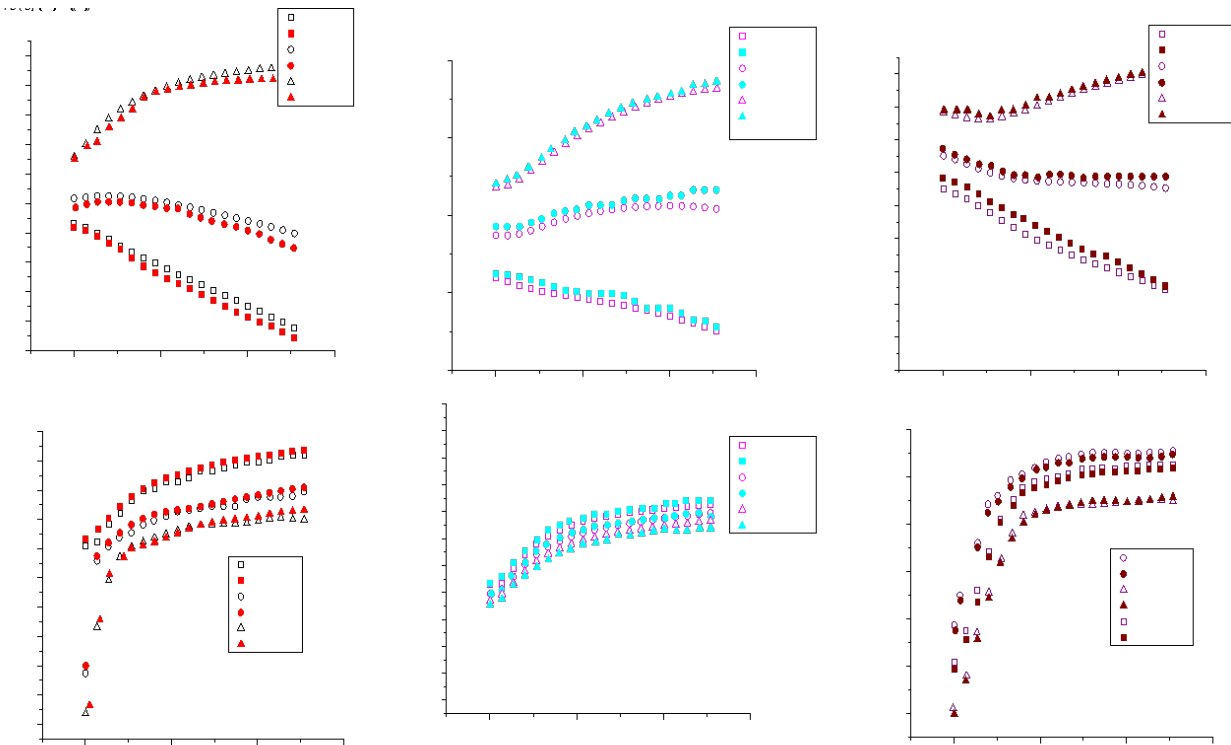


Figure 9: Age-opening angle for left and right arteries

### 3.1.2 1<sup>st</sup> Generation Data

Axial force and external radius data are plotted as functions of inflating pressure for each of the different longitudinal pre-stretch levels (Figure 10). External radius was found to increase with pressure while axial force presented a pre-stretch dependent behavior. The radius curve shapes displayed a biphasic pattern; the initial phase occurred at low pressures, namely from 0 to approximately 4kPa, and was characterized by a variation in radius, whereas the second phase, occurring at higher pressures, was accompanied by establishing these dimensions. Conversely, axial force exhibited limited range values at low pressures and a wide range at high pressures. Increasing the level of pre-stretch resulted in a shift towards higher forces but lower radius, a behavior attributed to Poisson effect.



**Figure 10: Axial force and external radius data as functions of inflating pressure for left and right arteries (left), female and male samples (middle) and young (<45 y.o.) and old (>45 y.o.) samples (right)**

### 3.1.3 2<sup>nd</sup> Generation Data

Figure 11 shows circumferential and longitudinal Cauchy stresses as a function of circumferential stretches. Increasing the level of longitudinal pre-stretch resulted in the curve shifting leftward, as a result of the Poisson effect. The lumen pressure against force and lumen pressure against radius plots are constructed by the use of equations A7 and A8 of Appendix A2.

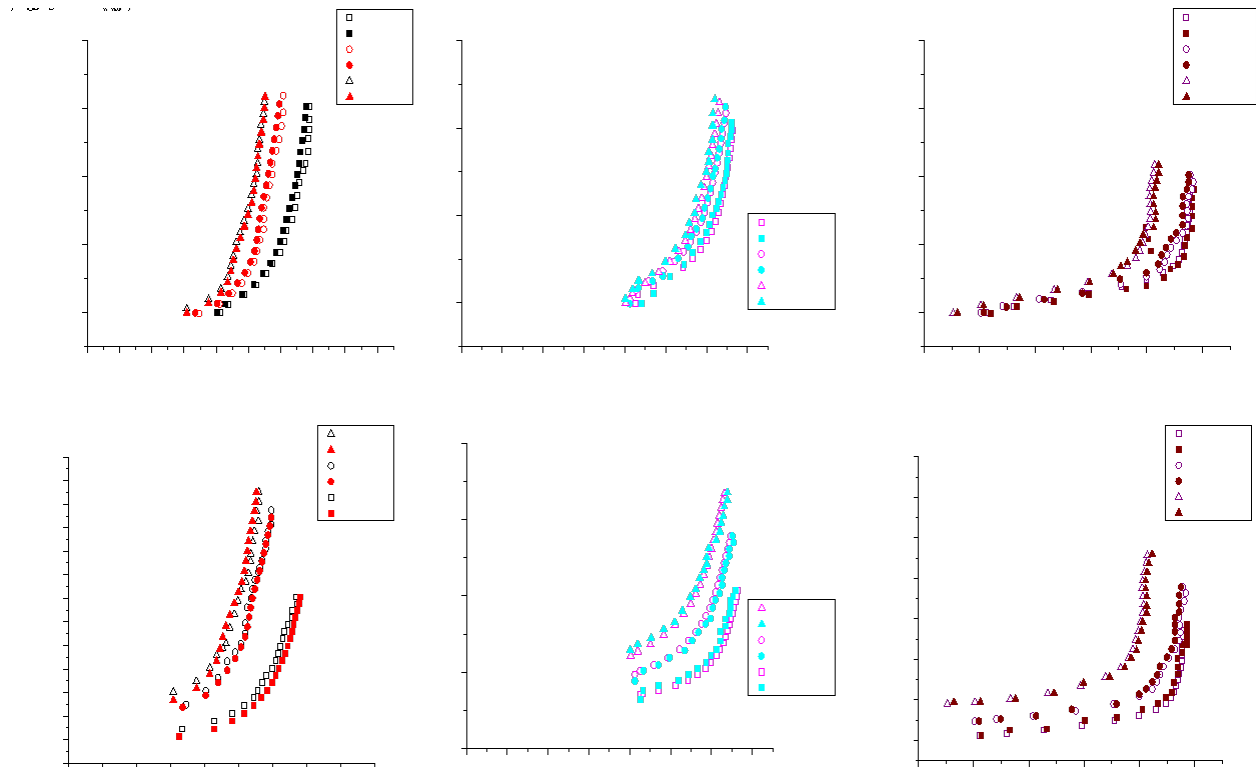


**Figure 11: Circumferential and Longitudinal Cauchy stresses as a function of circumferential stretches for left and right arteries (left), female and male samples (middle) and young (<45 y.o.) and old (>45 y.o.) samples (right)**

Representative circumferential and longitudinal stress as a function of circumferential strain data of left and right renal data from a male sample are shown in Figure 12. Non-significant gender differences were revealed. Regional differences were observed among left and right arteries of both male and female samples, with left renal arteries being stiffer and less compliant.

All SEFs were simulated adequately ( $R^2 > 0.90$ ), but the biphasic SEF (quadratic and Fung – type SEF) afforded the most accurate simulation. Fung- type SEF offered poor simulation both to the circumferential and longitudinal data. Neo-Hookean and Fung – type SEF underestimated the low - stress longitudinal data; while it captured properly the circumferential stress data. Finally, the quadratic and Fung – type SEF afforded superior fit to all data. Via the quadratic term, the biphasic model afforded improved simulations of low – stress data and via the exponential term captured the normal and high stress data.

Table 2 (see section 3.2.2) lists the model parameters optimised, as well as the RMS errors  $\epsilon$  and the determinants of the correlation matrix of material parameters  $\det(R)$  computed.

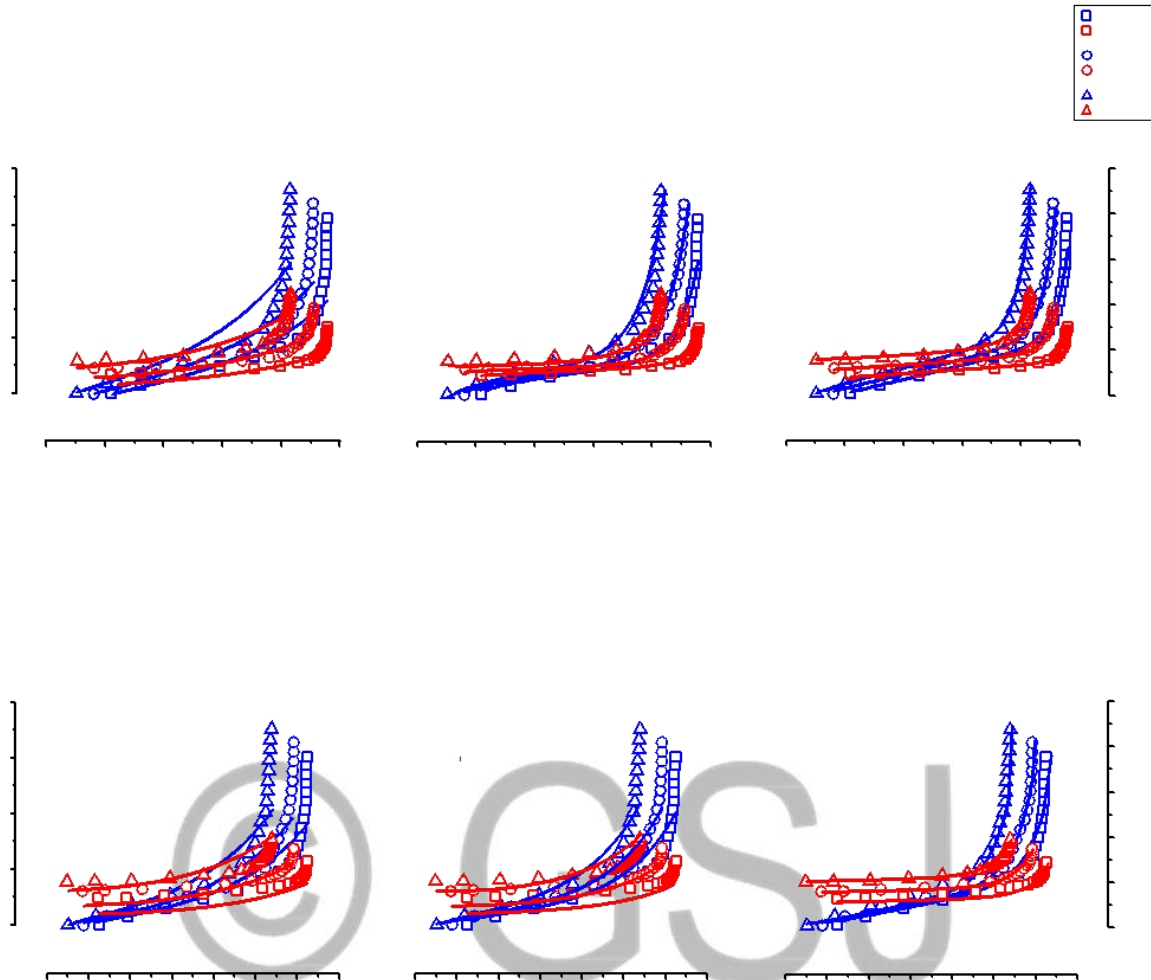


**Figure 12: Representative circumferential (red) and longitudinal (blue) stress vs. circumferential strain data of left and right renal data from a male sample**

### 3.2 Simulation Results

In this section, the experiment of the applied axial and circumferential stretch is compared with the corresponding simulations. The rationale behind using a customized material produced from the experimental data is explained and the mesh independence is presented.

#### 3.2.1 Neoprene Rubber Test

First, the response of a ready-to-go material from the ANSYS engineering library data called Neoprene Rubber (ANSYS, 19.2) is examined. This material is hyperelastic and isotropic with incompressible behavior which is suitable for the simulation. The advantage is that the following simulations would have the same formation except from the used material that would be the user customized.

Figure A2 in Appendix 3 presents the Neoprene Rubber response under an axial stretch of 20% and a following deformation through the application of internal pressure at 26 kPa. As it can be observed, the material could not handle the total applied pressure load, which led to a non-converging solution. More specifically, the material received only 36% of the total pressure until the simulation termination. Based on this, it was decided that the use of a user defined material was necessary in order to simulate a stiffer behavior and have a better response to higher loads.

### 3.2.2 Mesh independence

Figure 13 shows the simulation stress-strain curves for 20% axial stretch and an internal pressure of 26kPa for three different mesh sizes. The normal mesh is generally constructed with an average element size of 0.10mm. The coarse mesh is approximately 15% smaller on the total number of elements than the normal one, with an average element size of 0.11mm, while the fine one is 18% bigger on the total number of elements, with an average element size of 0.09mm. For the coarse mesh the required RAM is 8% less than the normal and 24% more in the fine mesh. Regarding the computational time, the coarse mesh needs 4% less time, and the fine mesh needs 154% more time, compared to the normal. Finally, the differences between the computed values for the strain and stress are below 1% (Table 2).



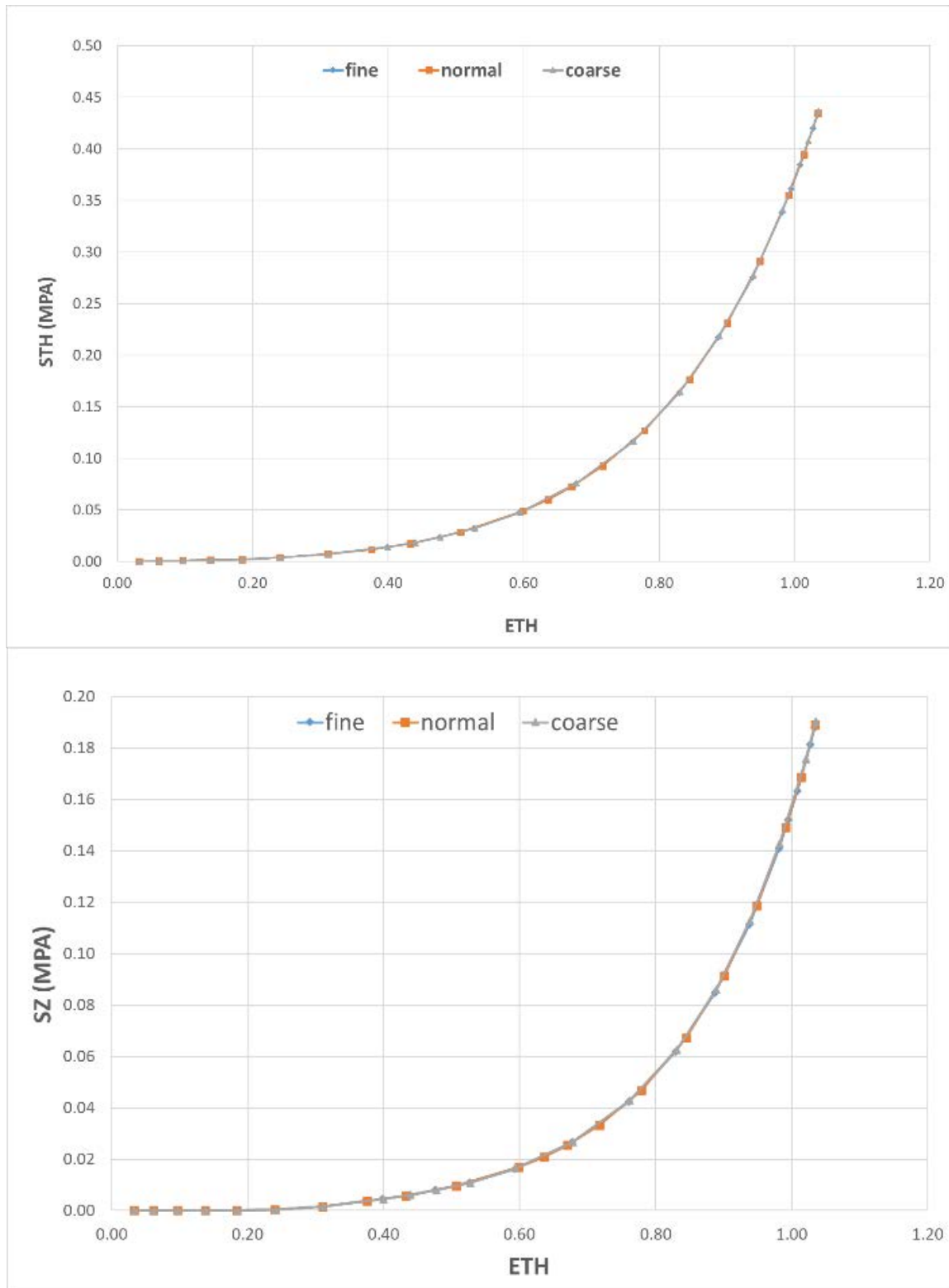


Figure 13: Mesh independence for circumferential stresses (top) and axial (bottom) stresses

Table 2: Mesh independence compare values

	Normalized Values (%)	Eth	Sth	Sz	Time	RAM	Element Number
Mesh Type	Normal	100	100	100	100	100	100
	Fine	99.94	99.61	99.42	254.17	124.9	118.11
	Coarse	100.08	100.46	100.69	95.83	91.82	84.63

Taking into account the coarse and fine mesh requirements for computational time and memory in anticipation with the results differences, which are considered reasonable for this research analysis, the normal mesh is chosen in order to be used in the following simulations.

### 3.2.3 Simulations

Figures 14-19 show the comparison of the model response with the experimental data for 20%, 40% and 50% axial stretch, followed by internal pressure loading until 26kPa.

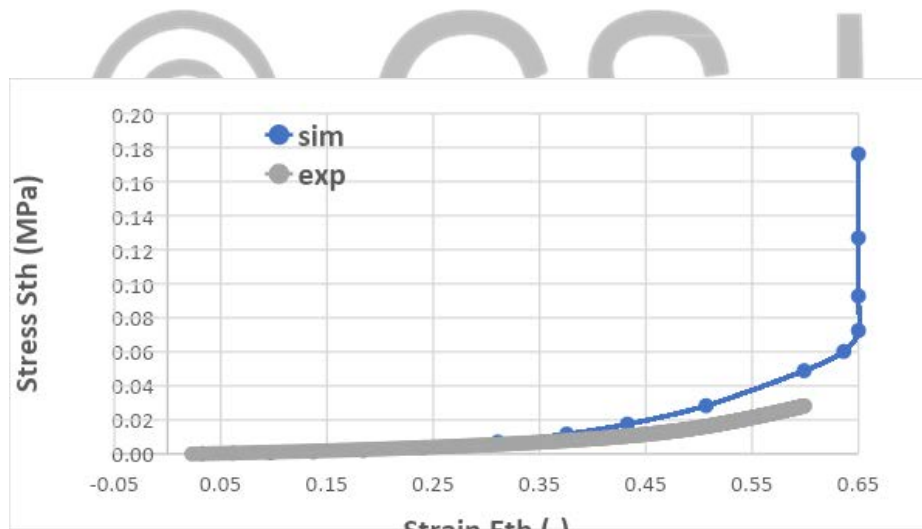


Figure 14: Circumferential Stress-strain curves for experimental versus simulated values for  $\lambda=1.2$

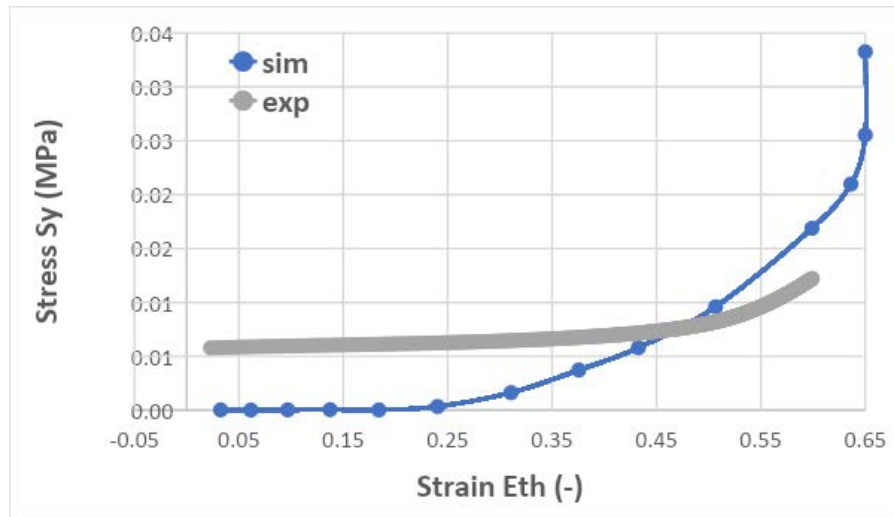


Figure 15: Axial Stress-strain curves for experimental versus simulated values for  $\lambda=1.2$

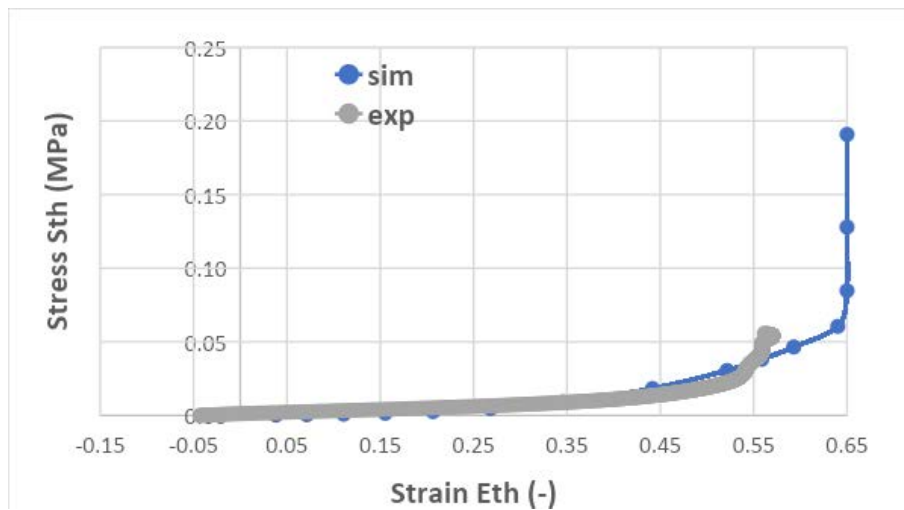


Figure 16: Circumferential Stress-strain curves for experimental versus simulated values for  $\lambda=1.4$

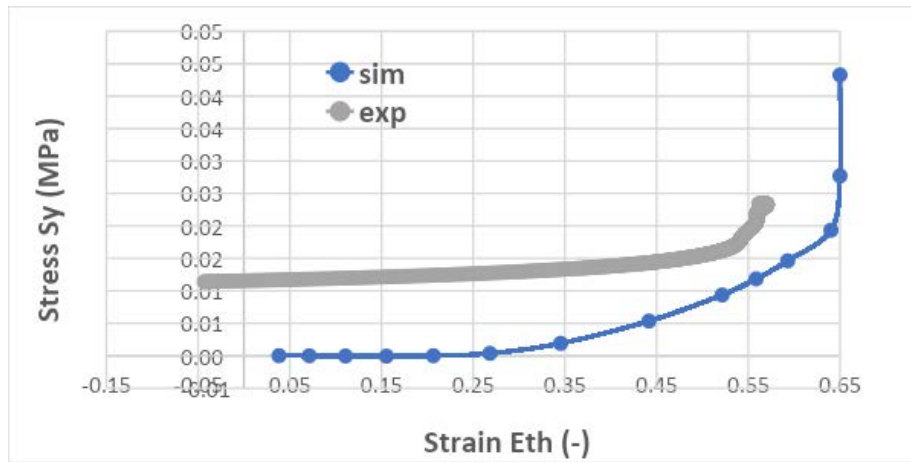


Figure 17: Axial Stress-strain curves for experimental versus simulated values for  $\lambda=1.4$

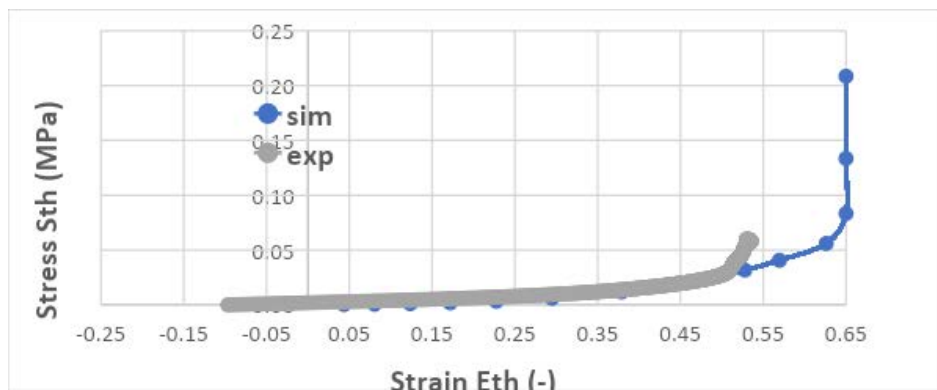


Figure 18: Circumferential Stress-strain curves for experimental versus simulated values for  $\lambda=1.5$

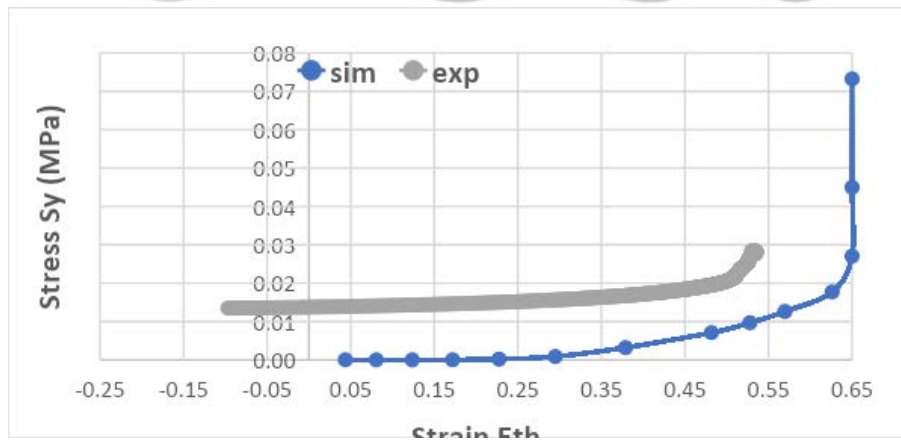


Figure 19: Axial Stress-strain curves for experimental versus simulated values for  $\lambda=1.5$

#### 4. Discussion on results and conclusions

Biomechanical properties of arteries have been under scrutiny over the last decades. Experimental research is necessary in order to examine the mechanical properties in relation to structural and functional changes; however, fresh human tissues are scarce and difficult to obtain. To the best of our knowledge, this is the first study examining the mechanical properties of human renal arteries with respect to functionality, material characterization and presenting a computational model to interrogate aspects of the mechanical behaviour of the renal arteries not possible to examine experimentally.

The analysis has shown a strong correlation between the opening angle and the residual strains in the outer surface regarding all renal arteries (independent from gender). There was no correlation between the opening angle and the residual strains in the inner surface and very good correlation between the difference of the residual strains (outer surface-inner surface), independently to gender difference. Residual stresses have a crucial role in the vascular mechanical behavior. Inner walls exhibit residual compressive strains while outer walls exhibit residual tensile strains; these “opposing” residual strains contribute to equalize the stress through the wall due to internal pressure. The compressed intima is thus better protected from the luminal flow.

With respect to the relationship between opening angle and age, the results revealed that there was strong negative correlation in male subjects and in the right arteries. Several studies in the literature have demonstrated that ageing is associated with arterial stiffening. However, this relationship has been established for large elastic arteries, and there has been no conclusive evidence provided on the behavior of muscular arteries (Borlotti et al., 2012; Leloup et al., 2015; Ruitenbeek et al., 2008; Zhang et al., 2013). It has also been reported that elastic lamellae undergo fatigue and progressive fragmentation occurs with time; this phenomenon is believed to be predominant in the elastic arteries due to high stretch amplitude (O’Rourke and Hashimoto, 2007). Published data from an in-vitro study has shown that while indeed stiffness in elastic arteries increases with ageing, this pattern is not observed in muscular arteries (Mitchell et al., 2004). One limitation of the current study is the small number of samples which may have reduced the chance of detecting correlations in same-gender groups or in left renal arteries.

Radius versus luminal pressure relation shows that at the range of 0 to approximately 4kPa, the radius exhibits a precipitous increase which is moderated at higher pressures, in fact almost flattening for pressures greater than 20kPa. Increasing levels of pre-stretch pushes the curve of radius-luminal pressure downwards and seems to lead to a faster shift in the load bearing towards the stiffer collagen substructure. This is in accordance with literature findings, as, at low pressures, the artery is predominantly supported by the crimped elastin fibers which are easily stretched and keep the loads evenly distributed throughout the tissue; at higher pressures the much stiffer – reported to approximately three orders of magnitude - collagen fibers are fully engaged and take the role of the main load-bearing component, in fact preventing the rupture of the artery at very high pressures (Chow et al., 2014).

Findings from the first-generation data (axial force versus lumen pressure and cylindrical radius versus lumen pressure) were similar for the left and right renal arteries. Incremental differences were demonstrated in the forces for male against female subjects, which may result to less arterial failures for females (Kander et al., 2017; Ryu et al., 2020). The same results were revealed for radius in female versus male subjects, presumably because of the higher mean size of males against females. When examining the role of age, again the incremental values may be explained by the quantity of elastin fibers that is responsible for the elastic tissue behavior. Through ageing, the elastin fibers collapse so the tissue cannot return to previous state without enforced actions (Fhayli et al., 2019).

The second-generation data follow the patterns of first generation data for all stretch ratios  $\lambda = 1.3, \lambda = 1.4, \lambda = 1.5$ . We also use phenomenological Strain Energy Function Fung-Quadratic that fitted very well to experimental data for stretch ratios  $\lambda = 1.3, \lambda = 1.4, \lambda = 1.5$  as we can conclude by numerical matrix of coefficients.

Regarding the simulation results, first it can be observed that only a user-defined material can overcome the load application and succeed at a converged solution. Furthermore, it should be noted that while, on one hand, the simulation results follow the experimental data, especially in small strains (below 0.5), on the other hand, a higher curve end is observed in the stress and strain value. This could be ascribed to the use of the error minimization tool which was employed for the translation of the material response. What is observed from the Figures 15, 17 and 19, which refer to the axial direction of stress, is a pattern of shifted curves of the experimental data compared to the simulation. This difference is attributed to the two-step simulation process where the pressure application is taking place at an advancing step, following the axial stretching, thereby leading to which zeroing of the axial stress condition. In the experiment, the sample is in an actual axial pre-stress condition due to stretching before pressure loading.

In this study, it was not possible to use a ready material with hyperelastic, isotropic, incompressible behavior like Neoprene Rubber, due to its inability to respond to high loads. In anticipation, a user defined material characterized based on biaxial experimental results, enabled producing an orthotropic, hyperelastic and near incompressible material. This material can overcome the aforementioned problem of high loads and achieve a converged state solution with acceptable results regarding the response of strain – stress curves. This observation verifies the initial identified need and scope of the experimental approach to construct a bio-material library.

The difference between simulation and experiment also supports the initial selection of using an orthotropic material instead of an isotropic one. This is also explained by the application of a Mooney-Rivlin instead of Neo-Hookean model, due to its capability of using biaxial data instead of only uniaxial in order to characterize the material, which consequently leads to an orthotropic behavior. Furthermore, a Mooney-Rivlin model can present a better behavior in large deformation states (above 100%). This is seen from the simulation stress-strain curves which range in the same order of magnitude with those that are produced from the experiments.

Overall, a major contribution of this study is the enrichment of the engineering material library regarding biomaterials. This could prove beneficial not only in structural cases but also in 2-way Fluid Structure Interaction (FSI) cases, where a biomaterial is acting simultaneously with a fluid, e.g. blood. Results regarding the material response to load application are supported by both a mathematical and software simulation approach, which further strengthens the quality of the material construction and characterization. In future studies, user-defined fitters could be applied in order to exploit experimental values and extract new materials that can eliminate the divergence between experimental and simulation procedures. Concerning the simulation procedure, a different model could also be applied for the strain energy function in order to describe the material response. The Mooney Rivlin model uses the first and second invariant of the left Cauchy-Green deformation tensor. MRI stacks of arteries can further be used in order to extract a 3D model that represents a real-life human tissue. Combining all of the above, a 2-way FSI simulation can be established and lead to more accurate results in order to observe and simulate many different situations from the in vivo status.

### **Acknowledgements**

Ethics were handled under the authority of the Presidential Decree No 56/2013, article 36; published in the Official Government Gazette on April 30, 2013. The authors acknowledge the Biomedical Research Foundation of the Academy of Athens (BRFAA), for the provision of the facilities of the Laboratory Biomechanics, Center of Clinical, Experimental Surgery, to conduct the experimental part of this research, as well as the Department of Forensic Medicine and Toxicology, Medical School, University of Athens, Athens, Greece, for providing the human cadaveric samples.

## References

- [1] Gulas E, Wyśiadecki G, Szymański J, Majos A, Stefańczyk L, Topol M, Polgaj M. Morphological and clinical aspects of the occurrence of accessory (multiple) renal arteries. *Archives of medical science: AMS*. 2018 Mar;14(2):442. <https://doi.org/10.5114/aoms.2015.55203>
- [2] Leslie, S.W., Sajjad, H. Anatomy, Abdomen and Pelvis, Renal Artery. [Updated 2019 Oct 21]. In: StatPearls [Internet]. Treasure Island (FL): StatPearls Publishing; 2020 Jan-. Available from: <https://www.ncbi.nlm.nih.gov/books/NBK459158/>
- [3] Chade, A.R. (2014). Microvascular Disease. In Lilach O. Lerman & Stephen C. Textor (Eds.), *Renal Vascular Disease* (pp. 132-133). Springer-Verlag.
- [4] Climie RE, Gallo A, Picone DS, Di Lascio N, Van Sloten TT, Guala A, Mayer CC, Hametner B, Bruno RM. Measuring the interaction between the macro-and micro-vasculature. *Frontiers in cardiovascular medicine*. 2019 Nov 22;6:169. <https://doi.org/10.3389/fcvm.2019.00169>
- [5] Textor SC, Lerman L, McKusick M. The uncertain value of renal artery interventions: where are we now?. *JACC: Cardiovascular Interventions*. 2009 Mar;2(3):175-82. <https://doi.org/10.1016/j.jcin.2008.12.008>
- [6] Herrmann SM, Textor SC. Current concepts in the treatment of renovascular hypertension. *American journal of hypertension*. 2018 Jan 12;31(2):139-49. <https://doi.org/10.1093/ajh/hpx154>
- [7] Calabia J, Torguet P, Garcia I, Martin N, Mate G, Marin A, Molina C, Valles M. The relationship between renal resistive index, arterial stiffness, and atherosclerotic burden: the link between macrocirculation and microcirculation. *The Journal of Clinical Hypertension*. 2014 Mar;16(3):186-91. <https://doi.org/10.1111/jch.12248>
- [8] Zanolli L, Lentini P, Briet M, Castellino P, House AA, London GM, Malatino L, McCullough PA, Mikhailidis DP, Boutouyrie P. Arterial stiffness in the heart disease of CKD. *Journal of the American Society of Nephrology*. 2019 Jun 1;30(6):918-28. <https://doi.org/10.1681/ASN.2019020117>
- [9] American Heart Association – American Stroke Association (2017). Cardiovascular disease: a costly burden for America. Projections through 2035. <https://healthmetrics.heart.org/cardiovascular-disease-a-costly-burden/>
- [10] Fung, YC. *Biomechanics: Mechanical properties of living tissues*, 2<sup>nd</sup> edn. New York, NY: Springer-Verlag, 1993.
- [11] Humphrey JD, Na S. Elastodynamics and arterial wall stress. *Annals of biomedical engineering*. 2002 Apr;30(4):509-23. <https://doi.org/10.1114/1.1467676>
- [12] Butlin M, Tan I, Spronck B, Avolio AP. Measuring Arterial Stiffness in Animal Experimental Studies. *Arteriosclerosis, thrombosis, and vascular biology*. 2020 May;40(5):1068-77. <https://doi.org/10.1161/ATVBAHA.119.313861>
- [13] Vappou J, Luo J, Konofagou EE. Pulse wave imaging for noninvasive and quantitative measurement of arterial stiffness in vivo. *American journal of hypertension*. 2010 Apr 1;23(4):393-8. <https://doi.org/10.1038/ajh.2009.272>
- [14] Avril S, Badel P, Gabr M, Sutton MA, Lessner SM. Biomechanics of porcine renal arteries and role of axial stretch. *Journal of biomechanical engineering*. 2013 Aug 1;135(8). <https://doi.org/10.1115/1.4024685>
- [15] Zhou B, Wolf L, Rachev A, Shazly T. A structure-motivated model of the passive mechanical response of the primary porcine renal artery. *Journal of Mechanics in Medicine and Biology*. 2014 Jun 12;14(03):1450033. <https://doi.org/10.1142/S021951941450033X>
- [16] Guo X, Lu X, Kassab GS. Transmural strain distribution in the blood vessel wall. *American Journal of Physiology-Heart and Circulatory Physiology*. 2005 Feb;288(2):H881-6. <https://doi.org/10.1152/ajpheart.00607.2004>
- [17] Sokolis DP. Multiaxial mechanical behaviour of the passive ureteral wall: experimental study and mathematical characterisation. *Computer methods in biomechanics and biomedical engineering*. 2012 Nov 1;15(11):1145-56. <https://doi.org/10.1080/10255842.2011.581237>
- [18] Sokolis DP. Experimental investigation and constitutive modeling of the 3D histomechanical properties of vein tissue. *Biomechanics and modeling in mechanobiology*. 2013 Jun;12(3):431-51. PMID: 22706981.
- [19] Zhou J, Fung YC. The degree of nonlinearity and anisotropy of blood vessel elasticity. *Proceedings of the National Academy of Sciences*. 1997 Dec 23;94(26):14255-60. <https://doi.org/10.1073/pnas.94.26.14255>
- [20] Fung YC, Fronek K, Patitucci P. Pseudoelasticity of arteries and the choice of its mathematical expression. *American Journal of Physiology-Heart and Circulatory Physiology*. 1979 Nov 1;237(5):H620-31. <https://doi.org/10.1152/ajpheart.1979.237.5.H620>

- [21] Weizsacker HW, Pinto JG. Isotropy and anisotropy of the arterial wall. *Journal of biomechanics*. 1988 Jan 1;21(6):477-87. [https://doi.org/10.1016/0021-9290\(88\)90240-0](https://doi.org/10.1016/0021-9290(88)90240-0)
- [22] Li W. Biomechanical property and modelling of venous wall. *Progress in biophysics and molecular biology*. 2018 Mar 1;133:56-75. <https://doi.org/10.1016/j.pbiomolbio.2017.11.004>
- [23] Scotti CM, Jimenez J, Muluk SC, Finol EA. Wall stress and flow dynamics in abdominal aortic aneurysms: finite element analysis vs. fluid–structure interaction. *Computer methods in biomechanics and biomedical engineering*. 2008 Jun 1;11(3):301-22. <https://doi.org/10.1080/10255840701827412>
- [24] Stolarski H, Belytschko T. Shear and membrane locking in curved CO elements. *Computer methods in applied mechanics and engineering*. 1983 Dec 1;41(3):279-96. [https://doi.org/10.1016/0045-7825\(83\)90010-5](https://doi.org/10.1016/0045-7825(83)90010-5)
- [25] Wells GN, Sluys LJ, De Borst R. A p-adaptive scheme for overcoming volumetric locking during plastic flow. *Computer Methods in Applied Mechanics and Engineering*. 2002 May 10;191(29-30):3153-64. DOI:10.1016/S0045-7825(02)00252-9.
- [26] Borlotti A, Khir AW, Rietzschel ER, De Buyzere ML, Vermeersch S, Segers P. Noninvasive determination of local pulse wave velocity and wave intensity: changes with age and gender in the carotid and femoral arteries of healthy human. *Journal of applied physiology*. 2012 Sep 1;113(5):727-35. <https://doi.org/10.1152/jappphysiol.00164.2012>
- [27] Leloup AJ, Van Hove CE, Heykers A, Schrijvers DM, De Meyer GR, Franssen P. Elastic and muscular arteries differ in structure, basal NO production and voltage-gated Ca<sup>2+</sup>-channels. *Frontiers in physiology*. 2015 Dec 15;6:375. <https://doi.org/10.3389/fphys.2015.00375>
- [28] Ruitenbeek AG, Van Der Cammen TJ, Van Den Meiracker AH, Mattace-Raso FU. Age and blood pressure levels modify the functional properties of central but not peripheral arteries. *Angiology*. 2008 Jun;59(3):290-5. <https://doi.org/10.1177/0003319707305692>
- [29] Zhang Y, Agnoletti D, Protogerou AD, Topouchian J, Wang JG, Xu Y, Blacher J, Safar ME. Characteristics of pulse wave velocity in elastic and muscular arteries: a mismatch beyond age. *Journal of Hypertension*. 2013 Mar 1;31(3):554-9. DOI: [10.1097/HJH.0b013e32835d4aec](https://doi.org/10.1097/HJH.0b013e32835d4aec)
- [30] O’rourke MF, Hashimoto J. Mechanical factors in arterial aging: a clinical perspective. *Journal of the American College of Cardiology*. 2007 Jul 3;50(1):1-3. DOI:10.1016/j.jacc.2006.12.050
- [31] Mitchell GF, Parise H, Benjamin EJ, Larson MG, Keyes MJ, Vita JA, Vasani RS, Levy D. Changes in arterial stiffness and wave reflection with advancing age in healthy men and women: the Framingham Heart Study. *Hypertension*. 2004 Jun 1;43(6):1239-45. <https://doi.org/10.1161/01.HYP.0000128420.01881.a>
- [32] Chow MJ, Turcotte R, Lin CP, Zhang Y. Arterial extracellular matrix: a mechanobiological study of the contributions and interactions of elastin and collagen. *Biophysical journal*. 2014 Jun 17;106(12):2684-92. <https://doi.org/10.1016/j.bpj.2014.05.014>
- [33] Kander MC, Cui Y, Liu Z. Gender difference in oxidative stress: a new look at the mechanisms for cardiovascular diseases. *Journal of cellular and molecular medicine*. 2017 May;21(5):1024-32. <https://doi.org/10.1111/jcmm.13038>
- [34] Ryu H, Moon J, Jung J. Sex differences in cardiovascular disease risk by socioeconomic status (SES) of workers using National health information database. *International journal of environmental research and public health*. 2020 Jan;17(6):2047. <https://doi.org/10.3390/ijerph17062047>
- [35] Fhayli W, Boëté Q, Harki O, Briançon-Marjollet A, Jacob MP, Fauray G. Rise and fall of elastic fibers from development to aging. Consequences on arterial structure-function and therapeutical perspectives. *Matrix Biology*. 2019 Nov 1;84:41-56. <https://doi.org/10.1016/j.matbio.2019.08.005>
- [36] ANSYS, 19.2. ANSYS Inc. [Online] Available at: <https://www.ansys.com/>
- [37] Brasen JC, de Wit C, Sorensen CM. Myoendothelial coupling through Cx40 contributes to EDH-induced vasodilation in murine renal arteries: evidence from experiments and modelling. *Acta Physiologica*. 2018 Jan;222(1):e12906. <https://doi.org/10.1111/apha.12906>
- [38] Coghlan KM, Breen LT, Martin Z, O’Neill S, Madhavan P, Moore D, Murphy BP. An experimental study to determine the optimal access route for renal artery interventions. *European Journal of Vascular and Endovascular Surgery*. 2013 Aug 1;46(2):236-41. <https://doi.org/10.1016/j.ejvs.2013.05.001>
- [39] DEMIRAY H, WEIZSACKER H, PASCALE K. A mechanical model for passive behaviour of rats carotid artery. *Biomedizinische Technik*. 1986;31(3):46-52. <https://doi.org/10.1515/bmte.1986.31.3.46>
- [40] Greenwald SE. Ageing of the conduit arteries. *The Journal of Pathology: A Journal of the Pathological Society of Great Britain and Ireland*. 2007 Jan;211(2):157-72. <https://doi.org/10.1002/path.2101>

- [41] Kim B, Lee SB, Lee J, Cho S, Park H, Yeom S, Park SH. A comparison among Neo-Hookean model, Mooney-Rivlin model, and Ogden model for chloroprene rubber. *International Journal of Precision Engineering and Manufacturing*. 2012 May 1;13(5):759-64. <https://doi.org/10.1007/s12541-012-0099-y>
- [42] Lima A, van Rooij T, Ergin B, Sorelli M, Ince Y, Specht PA, Mik EG, Bocchi L, Kooiman K, de Jong N, Ince C. Dynamic contrast-enhanced ultrasound identifies microcirculatory alterations in sepsis-induced acute kidney injury. *Critical care medicine*. 2018 Aug 1;46(8):1284-92. <https://doi.org/10.1097/CCM.0000000000003209>
- [43] Mazensky D, Flesarova S. Arrangement of renal arteries in guinea pig. *The Anatomical Record*. 2017 Mar;300(3):556-9. <https://doi.org/10.1002/ar.23496>
- [44] Duch BU, Petersen JA, Vinter-Jensen L, Gregersen H. Elastic properties in the circumferential direction in isolated rat small intestine. *Acta physiologica scandinavica*. 1996 Jun;157(2):157-63. <https://doi.org/10.1046/j.1365-201X.1996.503248000.x>

© GSJ

## Appendix 1

**Table A1: Cadaver sampling metadata (L: left, R: right, M: male, F: female, Y: Yes, N: No)**

Case Number	Artery	Gender	Age	Reason of death	Heart mass	Level of coronal disease	Valve status	Hypertension	Smoking	Diabetes
1	L & R	M	61	Heart attack	normal	90%	none	N	Y	Y
2	L & R	F	56	Unknown	increased (520 g)	75%	Calcifications aortic stenosis	Y	Y	N
3	R	M	24	Car accident	normal	none	none	N	N	N
4	L & R	F	24	Car accident	normal	25%	none	N	Y	N
5	L	F	90	Unknown	increased (500 g)	75%	Calcifications	Y	N	Y
6	R	F	90	Unknown	increased (500 g)	90%	Calcifications	Y	N	Y
7	L	M	65	Heart attack	increased (520 g)	75%	none	Y	Y	Y
8	L	M	51	Ischemic of myocardium	normal	90%	None - relative cardiovascular disease	Y	not for the last 1 year	Y
9	L & R	F	42	Fall from height	normal	50%	none	Y	unknown	unknown
10	L & R	M	29	Drown	normal	75%	none	unknown	N	N
11	L & R	M	42	Heart attack	increased (500 g)	none	none	Y	N	N

**Table A2: Parameters of the SEF optimized to the experimental pressure-diameter-force data of renal artery**

	Specimen No	K[kPa]	b11[kPa]	b22[kPa]	b12[kPa]	Czz[-]	C88[-]	C8z[-]	ε[-]	R <sup>2</sup>	detR
RIGHT	1	0	8.221	8.964	4.671	25.711	76.942	17.855	0.202	0.94	8.70E-06
	2	15.371	14.48	33.502	26.081	14.264	8.56E-09	47.926	0.154	0.93	1.30E-06
	3	0.082	0	17.433	11.024	1.882	64.623	18.171	0.191	0.94	3.00E-06
	4	0.01	22.637	23.041	45.72	21.83	35.797	2.46E-06	0.426	0.74	3.40E-08
	5	0.003	10.203	12.582	3.001	3.382	17.271	4.86E-07	0.095	0.99	1.50E-05
	6	0.808	1.291	10.253	0	0.576	4.498	3.331	0.225	0.92	1.20E-06
	7	0	33.035	12.729	39.453	8.183	17.034	1.17E-05	0.404	0.72	7.60E-06
	8	3.228	3.392	0	0	4.555	3.444	5.066	0.284	0.89	5.40E-10
		<b>Mean</b>	2.438	11.657	14.813	16.244	10.048	27.451	11.544	0.248	0.885
	<b>S.E.</b>	1.889	4.034	3.555	6.504	3.371	10.325	5.85	0.041	0.035	
LEFT	1	0.004	0	24.958	0	0.448	51.508	19.115	0.245	0.92	2.00E-06
	2	1.363	4.006	17.515	6.375	0	8.52	13.639	0.158	0.96	4.30E-07
	3	0.021	39.406	19.382	45.699	7.459	12.522	0	0.394	0.78	7.30E-09
	4	0.033	61.554	33.169	91.257	12.063	34.627	0	0.462	0.66	1.20E-08
	5										
	6	2.397	19.425	27.001	0	0	12.764	14.711	0.137	0.97	2.60E-08
	7	1.837	9.677	0	1.444	2.829	4.599	4.489	0.322	0.84	8.20E-11
	8	0.536	17.538	13.076	52.627	1.562	18.32	0	0.5	0.52	1.20E-09
	9	0.071	30.791	40.521	0	0.687	36.462	43.875	0.192	0.89	
		<b>Mean</b>	0.783	22.8	21.953	24.675	3.131	22.415	11.979	0.301	0.819
	<b>S.E.</b>	0.337	7.228	4.416	12.216	1.546	5.842	5.287	0.049	0.056	

## Appendix 2

### 2.1 Kinematics

The principal extension ratios,  $\lambda_\theta$ ,  $\lambda_z$ , and  $\lambda_r$  were as follows:

$$\lambda_\theta = \frac{\pi r}{\theta R}$$

Equation A1

$$\lambda_z = \frac{l}{L}$$

Equation A2

The right-hand side of the radial component  $\lambda_r$ , was calculated using the incompressibility hypothesis.

$$\lambda_r = \frac{\partial r}{\partial R} = \frac{\theta RL}{\pi r l}$$

Equation A1

describing the circumferential  $\theta$ , longitudinal  $z$ , and radial  $r$  axes, deformations  $L$  and  $l$  were the respective lengths of the segment, and  $R$  and  $r$  were the radial positions of a material particle in the zero stress and loaded states, respectively, while  $\theta = \pi - a$ , where  $a$  is the opening angle.

The non-vanishing components of the Green strain tensor were as follows:

$$E_j = \frac{1}{2}(\lambda_j^2 - 1), j = \theta, z, r$$

Equation A4

Internal radius  $r_i$  was determined by integrating the previous equation.:

$$r_i = \sqrt{r_e^2 - (R_e^2 - R_i^2) \frac{\theta}{\lambda_z \pi}}$$

Equation A5

In relation to the external radius,  $r_e$ , as determined during the extension/inflation experiment, and the corresponding radii  $R_i$  and  $R_e$  at zero-stress state.

### 2.2 Constitutive formulations

As a result, differences in Cauchy stresses were recovered as:

$$\sigma_j - \sigma_r = \lambda_j^2 \frac{\partial \rho_0 w(E_\theta, E_z)}{\partial E_j} \quad j = \theta, z$$

Equation A6

Integrating the equilibrium equation in the r-axis,  $\frac{\partial \sigma_r}{\partial r} + \frac{\sigma_\theta - \sigma_r}{r} = 0$ , across thickness along with the boundary conditions, at inner surface  $\sigma_r|_{r=r_i} = -P$ , and external surface,  $\sigma_r|_{r=r_e} = 0$ , lumen pressure P was obtained. The lumen pressure P was calculated by integrating the equilibrium equation in the r-axis,  $\frac{\partial \sigma_r}{\partial r} + \frac{\sigma_\theta - \sigma_r}{r} = 0$ , through thickness and the boundary conditions at the inner surface,  $\sigma_r|_{r=r_i} = -P$ , and the external surface,  $\sigma_r|_{r=r_e} = 0$ .

$$P = \int_{r_i}^{r_e} \frac{\sigma_\theta - \sigma_r}{r} dr = \int_{r_i}^{r_e} \lambda_\theta^2 \frac{\partial \rho_0 w}{\partial E_\theta} \frac{dr}{r}$$

Equation A7

The integral of longitudinal stress over the wall cross-section on the two ends of the artery segment equals the sum of longitudinal force F and pressure force in the z direction, according to the equilibrium equation:

$$F = \pi \int_{r_i}^{r_e} [2(\sigma_z - \sigma_r) - (\sigma_\theta - \sigma_r)] r dr = \pi \int_{r_i}^{r_e} 2\lambda_z^2 \frac{\partial \rho_0 w}{\partial E_z} r dr - \pi \int_{r_i}^{r_e} 2\lambda_\theta^2 \frac{\partial \rho_0 w}{\partial E_\theta} r dr$$

Equation A8

For a thick-walled cylinder, stresses and strains are functions of the radius vector r. The following formulae give the average Cauchy stresses,  $\langle \sigma_\theta \rangle$ ,  $\langle \sigma_z \rangle$ , and  $\langle \sigma_r \rangle$  in the three axes, as well as the average circumferential extension ratio  $\langle \lambda_\theta \rangle$ :

$$\langle \sigma_\theta \rangle = \frac{pr_i}{r_e - r_i}$$

Equation A9

$$\langle \sigma_z \rangle = \frac{F + p\pi r_i^2}{\pi(r_e^2 - r_i^2)}$$

Equation A10

$$\langle \sigma_r \rangle = -\frac{pr_i}{r_e + r_i}$$

Equation A11

$$\langle \lambda_\theta \rangle = \frac{\pi(r_e + r_i)}{\theta(R_e + R_i)}$$

Equation A12

The upon formalism was adopted by relevant experimental methodology, Elastic Properties in the Circumferential Direction in Isolated Rat Small Intestine (Duch BU, 1996; Sokolis et al., 2013).

## Appendix 3

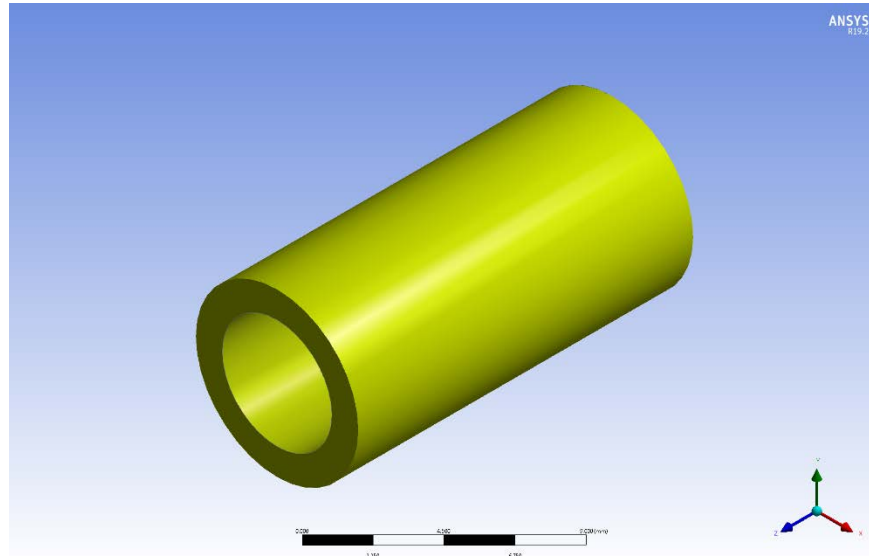


**Figure A1: 3D geometric model used in simulation procedure**

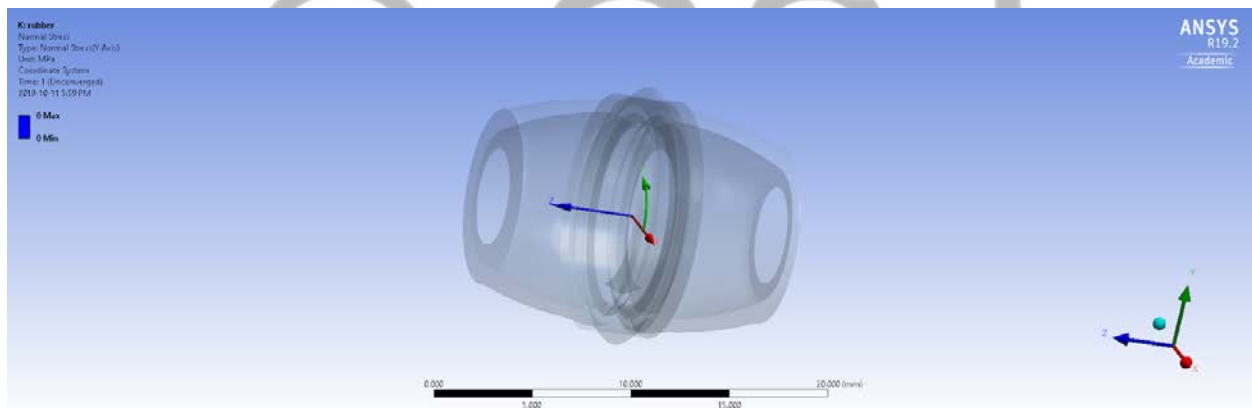


**Figure A2: Neoprene-Rubber material model under unconverged simulation**

## List of Figure and Table Captions

Figure 1: Fresh abdominal aorta from a 24 years old male after cleaning adherent tissues

Figure 2: The experimental set-up used for the inflation-extension testing

Figure 3: Material curve fitting in ANSYS Software

Figure 4: Computational domain discretization

Figure 5: Solution matrix

Figure 6: 1<sup>st</sup> step boundary conditions (top), 1<sup>st</sup> step pre-deformation state (middle) and 1<sup>st</sup> step after deformation state (bottom)

Figure 7: 2<sup>nd</sup> step boundary conditions (top), 2<sup>nd</sup> step pre-deformation state (middle), 2<sup>nd</sup> step post-deformation state (bottom)

Figure 8: Residual strain in outer wall (top) and difference in residual strain (outer-inner) (bottom), with differing opening angle

Figure 9: Age-opening angle for left and right arteries

Figure 10: Axial force and external radius data as functions of inflating pressure for left and right arteries (left), female and male samples (middle) and young (<45 y.o.) and old (>45 y.o.) samples (right)

Figure 11: Circumferential and Longitudinal Cauchy stresses as a function of circumferential stretches for left and right arteries (left), female and male samples (middle) and young (<45 y.o.) and old (>45 y.o.) samples (right)

Figure 12: Representative circumferential (red) and longitudinal (blue) stress vs. circumferential strain data of left and right renal data from a male sample

Figure 13: Mesh independence for circumferential stresses (top) and axial (bottom) stresses

Figure 14: Circumferential Stress-strain curves for experimental versus simulated values for  $\lambda=1.2$

Figure 15: Axial Stress-strain curves for experimental versus simulated values for  $\lambda=1.2$

Figure 16: Circumferential Stress-strain curves for experimental versus simulated values for  $\lambda=1.4$

Figure 17: Axial Stress-strain curves for experimental versus simulated values for  $\lambda=1.4$

Figure 18: Circumferential Stress-strain curves for experimental versus simulated values for  $\lambda=1.5$

Figure 19: Axial Stress-strain curves for experimental versus simulated values for  $\lambda=1.5$

Figure A1: 3D geometric model used in simulation procedure

Figure A2: Neoprene-Rubber material model under unconverged simulation

Table 1: Material constants obtained from the Mooney-Rivlin function.

Table 2: Mesh independence compare values

Table A1: Cadaver sampling metadata (L: left, R: right, M: male, F: female, Y: Yes, N: No)

Table A2: Parameters of the SEF optimized to the experimental pressure-diameter-force data of renal artery